Journal of Computational Applied Mechanics 2026, 57(4): 639-662

DOI: 10.22059/jcamech.2026.420632.1927

RESEARCH PAPER

Adaptive Fourier Feature Physics-Informed Neural Networks for Nonlinear Cattaneo–Vernotte Heat Conduction with Temperature-Dependent Properties

Shervin Shirmohamadi [a], Ali Fallah [b,*] , Mohammad Mohamadi Aghdam [a,†]

[a] *Mechanical Engineering Department, Amirkabir University of Technology, Tehran 15875-4413, Iran*
[b] *Department of Automotive Engineering, Faculty of Engineering, Atilim University, 06830, Ankara, Türkiye*

Abstract

In this study, Physics-Informed Neural Networks (PINNs) are employed as mesh-free solvers for nonlinear non-Fourier heat conduction governed by the Cattaneo–Vernotte (CV) equation with temperature-dependent thermal conductivity. The CV formulation accounts for finite thermal relaxation effects and leads to a hyperbolic heat conduction model, for which analytical solutions are generally unavailable in the nonlinear regime. Three PINN architectures are investigated: a standard PINN (S-PINN), a Fourier Feature PINN (F-PINN), and a novel Adaptive Fourier Feature PINN (AF-PINN). The models are systematically evaluated in both linear and nonlinear regimes and validated against analytical and high-resolution numerical reference solutions. The results demonstrate that fixed Fourier feature mappings substantially improve accuracy compared to standard PINNs; however, their performance is highly sensitive to the choice of spectral bandwidth and may deteriorate under non-optimal initialization, particularly in nonlinear cases. The proposed AF-PINN overcomes this limitation by dynamically adapting the Fourier bandwidth during training, yielding robust convergence across a wide range of initial conditions. Statistical analyses based on multiple random initializations confirm consistently low prediction error and reduced variance. Further examination of the optimization dynamics highlights the critical role of decoupled learning rates for the spectral scale and network weights in enabling recovery from adverse high-frequency initializations. Overall, the adaptive framework enhances the accuracy, stability, and robustness of PINN-based solvers for nonlinear non-Fourier heat transfer and provides a reliable foundation for modeling wave-dominated and multiscale thermal phenomena.

Keywords: Nonlinear heat conduction; Physics-Informed Neural Networks; Fourier Feature PINNs; Adaptive spectral learning.

1. Introduction

Classical heat conduction theory based on Fourier's law has been widely and successfully applied to a broad

* Corresponding author. Tel.: +90 (312) 586 8715. *E-mail address: Dr. Ali Fallah, Email: ali.fallah@atilim.edu.tr*

† Corresponding author. Tel.: +98-021-6454-3429. *E-mail address: Prof. Mohammad Mohamadi Aghdam, Email: Aghdam@aut.ac.ir*

range of engineering problems. However, the parabolic nature of the Fourier heat equation implies an infinite speed of thermal signal propagation, which becomes physically unrealistic when heat transfer occurs over extremely short time scales, at very high heat fluxes, or in micro- and nano-scale systems [1-4]. To overcome this limitation, non-Fourier heat conduction models have been proposed, among which the CV formulation is one of the most widely accepted extensions [5, 6]. By introducing a finite thermal relaxation time, the CV model transforms the governing heat equation from a parabolic to a hyperbolic form, allowing for finite thermal wave propagation [7].

The hyperbolic character of the CV equation introduces several distinctive features compared to classical Fourier heat conduction. In particular, the solution may exhibit wave-like behaviour, sharp transients, and strong sensitivity to initial and boundary conditions. These characteristics significantly increase the mathematical and numerical complexity of the problem [8]. The situation becomes even more challenging when material properties, such as thermal conductivity, are assumed to be temperature dependent. In this case, the governing equation becomes a nonlinear hyperbolic partial differential equation, for which analytical solutions are generally unavailable except for highly idealized configurations [9, 10].

Consequently, the solution of non-Fourier heat transfer problems with temperature-dependent properties relies primarily on numerical or semi-analytical methods [8, 11-14]. For instance, Rahideh et al. [12] presented a comprehensive numerical study of one- and two-dimensional CV heat conduction with temperature-dependent thermal conductivity using the incremental differential quadrature method (IDQM). Their work demonstrated that incorporating temperature dependence leads to strong nonlinear effects and significantly alters thermal wave propagation behavior, while also highlighting the high computational effort required for accurate numerical discretization. Building on this work, Saedodin et al. [8] investigated a one-dimensional nonlinear CV heat conduction problem using semi-analytical methods, including the reduced differential transform method (RDTM) and homotopy perturbation method (HPM). Although semi-analytical approaches can reduce computational cost, their applicability is typically restricted to simplified geometries, low-dimensional problems, and truncated series expansions that may lose accuracy at later times.

In recent years, artificial intelligence (AI) and machine learning techniques have attracted considerable attention in different fields of engineering such as material science [15], fluid mechanics [16], fault detection and condition monitoring [17, 18], computational mechanics [19] and heat and mass transfer modelling [20]. Data-driven neural networks have demonstrated remarkable success in approximating complex nonlinear mappings; however, their reliance on large, high-quality datasets limits their applicability in many engineering problems, where experimental or numerical data are scarce, expensive, or unavailable. In contrast, PINNs incorporate governing physical laws directly into the learning process by embedding differential equations, boundary conditions, and initial conditions into the loss function [21, 22]. This hybrid framework enables PINNs to solve both forward and inverse problems in a mesh-free manner while requiring minimal or no training data [22, 23]. To date, PINNs have been successfully applied to a wide range of engineering problems, including fluid mechanics [22], solid mechanics [24, 25], structural mechanics [26-29], and heat and mass transfer [30-32].

Despite their promise, standard or vanilla PINNs (i.e., S-PINNs) face notable challenges when applied to hyperbolic partial differential equations [33, 34]. The spectral bias of neural networks toward low-frequency solution components often leads to poor representation of sharp gradients and wave-like features inherent to non-Fourier heat conduction. To address this issue, F-PINNs have been proposed, where input coordinates are mapped into a higher-dimensional Fourier space to enhance the network's ability to capture high-frequency content [35]. Although F-PINNs have shown significant improvements in solving oscillatory and multiscale problems, their application to non-Fourier heat transfer remains largely unexplored. Several studies have demonstrated the effectiveness of PINNs for solving Fourier heat conduction problems, covering both forward and inverse formulations across one- and multi-dimensional domains [30-32, 36-40].

In contrast, applications of PINNs to non-Fourier heat conduction remain relatively scarce [41, 42]. For instance, Zheng et al. [42] investigated linear non-Fourier heat transfer using a hard-constraint physics-informed neural network (T-phPINN). Their approach employed two coupled subnetworks to approximate the temperature field and its first-order time derivative, enabling the network to better capture sharp thermal transients inherent to hyperbolic heat conduction models. The results demonstrated the feasibility of PINNs for solving one- and two-dimensional linear non-Fourier heat transfer problems. Similarly, Shi et al. [41] proposed a self-adaptive weight Physics-Informed Neural Network (SW-PINN) for linear non-Fourier heat conduction, in which the relative weights associated with the governing PDE, boundary conditions, and initial conditions are dynamically adjusted during training. Their findings further confirmed the capability of PINNs to handle non-Fourier heat transfer formulations.

Despite these advances, existing studies have primarily been limited to linear models with constant material properties. The applicability and robustness of current PINN formulations for more complex scenarios, such as temperature-dependent thermal conductivity, remain largely unexplored. Incorporating temperature-dependent properties introduces additional nonlinearity and strong coupling effects, which significantly increase the difficulty of the learning task and have not yet been systematically addressed within a PINN framework. Moreover, the potential benefits of adaptive Fourier feature strategies, in which the spectral representation of the neural network is dynamically adjusted during training, have not been investigated for nonlinear non-Fourier heat transfer problems.

In this study, a comprehensive PINN framework is developed for solving the Cattaneo–Vernotte non-Fourier heat conduction equation with temperature-dependent thermal conductivity. In addition to a standard PINN formulation, both a conventional Fourier Feature PINN and a novel Adaptive Fourier Feature PINN are implemented and systematically compared. The proposed framework aims to accurately capture thermal wave propagation and nonlinear effects in a mesh-free manner, without relying on predefined numerical grids. The performance of the different PINN variants is evaluated against analytical and high-resolution numerical reference solutions, with particular emphasis on accuracy, convergence behaviour, and robustness.

The main contributions of this study can be summarized as follows. First, a physics-informed neural network framework is developed for the solution of nonlinear CV non-Fourier heat conduction with temperature-dependent thermal conductivity, addressing a class of problems for which analytical solutions are generally unavailable. Second, the performance of S-PINNs, F-PINNs, and the novel AF-PINN is systematically investigated and compared in both linear and nonlinear regimes using analytical and numerical reference solutions. Third, an adaptive spectral learning strategy is introduced in which the Fourier bandwidth is treated as a learnable parameter and dynamically adjusted during training, eliminating the need for manual tuning and significantly enhancing robustness. Finally, a detailed analysis of the optimization dynamics reveals the critical role of decoupled learning rates for the spectral scale and network weights, enabling reliable recovery from adversarial high-frequency initializations and ensuring stable convergence for nonlinear non-Fourier heat transfer problems.

2. Governing Equations

In this study, non-Fourier heat conduction is modelled using the CV thermal wave formulation, which accounts for the finite speed of heat propagation by introducing a thermal relaxation time.

2.1. Energy conservation and constitutive relation

Consider a one-dimensional solid domain of length L, with spatial coordinate $x \in [0, L]$ and time $0 \le t$. The energy conservation equation is written as [8]:

$$\rho c_p \frac{\partial T(x,t)}{\partial t} + \frac{\partial q(x,t)}{\partial x} = 0, \tag{1}$$

where $T(x,t)$ is the temperature, $q(x,t)$ is the heat flux, ρ is the density, and c_p is the specific heat capacity.

To incorporate non-Fourier effects, the classical Fourier law is replaced by the Cattaneo–Vernotte constitutive equation,

$$\tau \frac{\partial q(x,t)}{\partial t} + q(x,t) + k(T) \frac{\partial T(x,t)}{\partial x} = 0, \tag{2}$$

where τ is the thermal relaxation time and $k(T)$ is the temperature-dependent thermal conductivity.

2.2. Nonlinear Cattaneo-Vernotte Heat Conduction

By combining the energy conservation equation with the CV constitutive relation, the governing heat conduction equation is obtained as

$$\frac{1}{\rho c_p} \frac{\partial k(T)}{\partial x} \frac{\partial T}{\partial x} + \frac{k(T)}{\rho c_p} \frac{\partial^2 T}{\partial x^2} = \frac{\partial T}{\partial t} + \tau \frac{\partial^2 T}{\partial t^2}. \tag{3}$$

This equation represents a nonlinear hyperbolic partial differential equation, where the second-order time derivative accounts for thermal wave propagation, and the nonlinearity arises from the temperature dependence of thermal conductivity. The thermal conductivity is assumed to vary linearly with temperature [8],

$$k(T) = k_0 \left[1 + \kappa \left(T - T_0 \right) \right], \tag{4}$$

where k_0 is the reference thermal conductivity at temperature T_0, and κ is the temperature-dependence coefficient.

2.3. Dimensionless formulation

To facilitate numerical implementation and parametric analysis, the governing equation is expressed in dimensionless form using the following nondimensional variables:

$$x = \frac{x}{L}, \qquad t = \frac{t}{t_{\text{total}}}, \qquad T = \frac{T}{T_0} \tag{5}$$

Additional dimensionless parameters are defined as

$$\alpha_0 = \frac{k_0}{\rho c_p}, \qquad \mathrm{Fo} = \frac{\alpha_0 t_{\text{total}}}{L^2}, \qquad \beta = \frac{\tau}{t_{\text{total}}}, \qquad \gamma = \kappa T_0 \tag{6}$$

Using these definitions, the dimensionless nonlinear Cattaneo–Vernotte equation becomes

$$\mathrm{Fo}c\left(\frac{\partial \tilde{T}}{\partial \tilde{x}}\right)^2 + \mathrm{Fo}\left[1+\gamma\left(\tilde{T}-1\right)\right]\frac{\partial^2 \tilde{T}}{\partial \tilde{x}^2} - \beta\frac{\partial^2 \tilde{T}}{\partial \tilde{t}^2} - \frac{\partial \tilde{T}}{\partial \tilde{t}} = 0. \tag{7}$$

This equation clearly highlights the combined effects of non-Fourier heat conduction and temperature-dependent material properties, resulting in a strongly nonlinear hyperbolic PDE.

2.4. Initial and boundary conditions

The problem is considered with the following homogeneous boundary and initial conditions:

$$T(0,t) = 0, \qquad T(L,t) = 0.$$
$$T(x,0) = \sin\left(\frac{\pi x}{L}\right), \qquad \frac{\partial T(x,0)}{\partial t} = 0. \tag{8}$$

3. Solution Procedure

3.1. Standard Physics-Informed Neural Network

Consider a general time-dependent partial differential equation defined over a spatial–temporal domain $\Omega \times (0,T]$,

$$\mathcal{F}\left(u(x,t), \nabla u(x,t), \nabla^2 u(x,t), \frac{\partial u}{\partial t}, \frac{\partial^2 u}{\partial t^2}\right) = 0, \qquad (x,t) \in \Omega \times (0,T], \tag{9}$$

subject to the following initial conditions,

$$u(x,0) = u_0(x), \qquad \frac{\partial u}{\partial t}(x,0) = v_0(x), \qquad x \in \Omega, \tag{10}$$

and boundary conditions,

$$\mathcal{B}\big(u(x,t)\big) = 0, \qquad (x,t) \in \partial\Omega \times (0,T], \tag{11}$$

where $u(x,t)$ is the unknown field variable, $\mathcal{F}(.)$ denotes the governing differential operator, and $\mathcal{B}(.)$ represents the boundary operator.

In the context of Physics-Informed Neural Networks, the unknown solution $u(x,t)$ is approximated by a neural network as [22]:

$$u(x,t) \approx \mathcal{N}_\theta(x,t), \tag{12}$$

where $\mathcal{N}_\theta$ is a fully connected feedforward neural network parameterized by weights and biases $\boldsymbol{\theta}$. The network takes the independent variables (x,t) as inputs and outputs the predicted solution field (**Figure 1**).

To enforce the governing physics, PINNs construct a composite loss function that penalizes violations of the differential equation, initial conditions, and boundary conditions. The total loss function is defined as

$$\mathcal{L}_{\text{PINN}} = \mathcal{L}_{\text{PDE}} + \mathcal{L}_{\text{IC}} + \mathcal{L}_{\text{BC}}. \tag{13}$$

The PDE residual loss enforces the governing equation at a set of collocation points $(x_f, t_f) \in \Omega \times (0,T]$,

$$\mathcal{L}_{\text{PDE}} = \frac{1}{N_f}\sum_{i=1}^{N_f}\left|\mathcal{F}\left(\mathcal{N}_\theta\left(x_f^{(i)}, t_f^{(i)}\right)\right)\right|^2, \tag{14}$$

where the required spatial and temporal derivatives are computed using automatic differentiation.

The initial-condition loss enforces both the initial field and its initial time derivative,

$$\mathcal{L}_{\text{IC}} = \frac{1}{N_{\text{ic}}}\sum_{i=1}^{N_{\text{ic}}}\left|\mathcal{N}_\theta\left(x_{\text{ic}}^{(i)},0\right) - u_0\left(x_{\text{ic}}^{(i)}\right)\right|^2 + \frac{1}{N_{\text{ic}}}\sum_{i=1}^{N_{\text{ic}}}\left|\frac{\partial \mathcal{N}_\theta}{\partial t}\left(x_{\text{ic}}^{(i)},0\right) - v_0\left(x_{\text{ic}}^{(i)}\right)\right|^2. \tag{15}$$

The boundary-condition loss is defined as

$$\mathcal{L}_{\text{BC}} = \frac{1}{N_{\text{bc}}}\sum_{i=1}^{N_{\text{bc}}}\left|\mathcal{B}\left(\mathcal{N}_\theta\left(x_{\text{bc}}^{(i)}, t_{\text{bc}}^{(i)}\right)\right)\right|^2. \tag{16}$$

In the present study, this general formulation is applied to the nonlinear CV heat conduction equation with temperature-dependent thermal conductivity, where the presence of second-order time derivatives and nonlinear spatial terms poses significant challenges for standard PINNs. In particular, the hyperbolic nature of the governing equation leads to wave-like solution features that are difficult to represent using conventional neural network architectures, motivating the use of Fourier feature-based enhancements introduced in the subsequent sections.

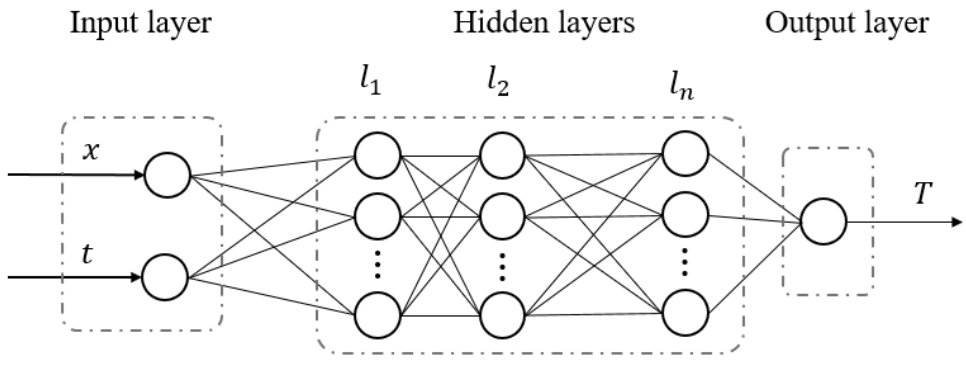

Figure 1: S-PINN architecture; A fully-connected neural network mapping (x, t) to T (x, t)

3.2. Fourier Feature Physics-Informed Neural Network

To address the limitations of standard PINNs in capturing high-frequency and wave-like solution components, F-PINNs enrich the input representation of the neural network by mapping the original coordinates into a higher-dimensional Fourier space [43]. This approach mitigates the spectral bias of neural networks and enhances their ability to approximate oscillatory and multiscale functions.

In the F-PINN framework, the original space–time input vector [44]:

$$\boldsymbol{\xi} = \left(\tilde{x}, \tilde{t}\right) \tag{17}$$

is first transformed using a Fourier feature mapping,

$$\gamma(\xi) = \left[\sin(\mathbf{B}\xi), \cos(\mathbf{B}\xi)\right] \tag{18}$$

where $\mathbf{B} \in R^{(m\times 2)}$ is a matrix of predefined frequencies, typically sampled from a Gaussian or uniform distribution, and m denotes the number of Fourier modes. The neural network then approximates the temperature field as:

$$\tilde{T}(\tilde{x},\tilde{t}) \approx \mathcal{N}_\theta(\gamma(\xi)) \tag{19}$$

with the same network architecture and output structure as the S-PINN, but operating in the transformed feature space (**Figure 2**).

The physics-informed loss function for the F-PINN retains the same structure as that of the S-PINN, including the PDE, initial, and boundary residuals. However, due to the enriched input representation, the F-PINN exhibits improved learning of sharp gradients and thermal wave propagation inherent to the CV model. This improvement is particularly important for cases involving temperature-dependent thermal conductivity, where nonlinearities further amplify high-frequency solution components.

Although Fourier feature embeddings significantly enhance expressiveness, their performance highly depends on the appropriate selection of frequency scales. Fixed Fourier features may still lead to suboptimal performance if the selected frequencies do not align well with the dominant spectral content of the solution. This limitation motivates the development of an adaptive Fourier Feature PINN, introduced in the next section.

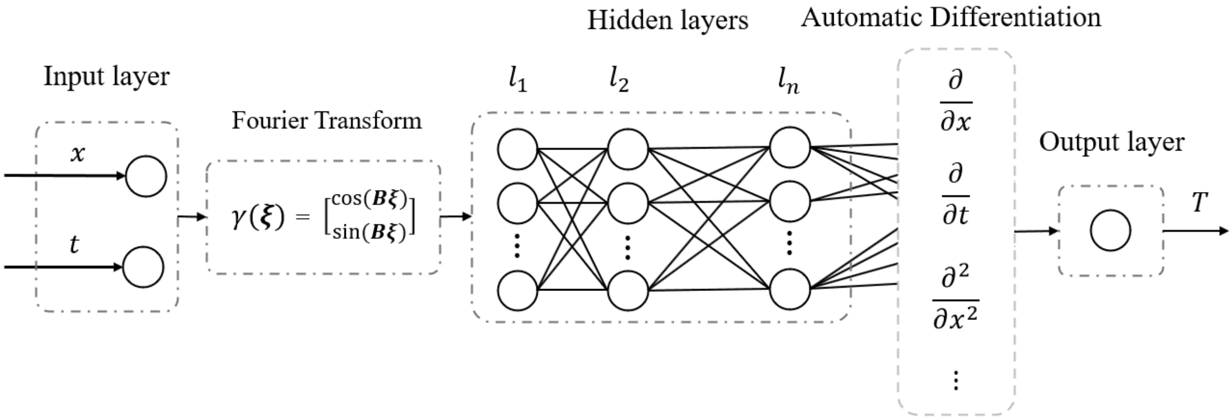

Figure 2: Network structure of F-PINN

3.3. Adaptive Fourier Feature Strategy

Although F-PINNs significantly enhance the representation capability of standard PINNs, their effectiveness depends strongly on the choice of the frequency matrix $\mathbf{B}$. In conventional F-PINNs, the frequencies are fixed at a priori and remain unchanged throughout the training process. However, for nonlinear and hyperbolic problems such as the CV heat conduction equation with temperature-dependent thermal conductivity, the dominant spectral content of the solution may evolve during training and vary across space and time. As a result, fixed Fourier features may not optimally align with the solution spectrum, leading to suboptimal convergence or unnecessary training stiffness. To address this limitation, an AF-PINN framework is developed in this study. The central idea of the adaptive approach is to update the Fourier feature frequencies during the training process, allowing the network to dynamically adjust its spectral representation in response to the evolving solution characteristics.

In the proposed framework, the Fourier feature mapping retains the same functional form as in the standard F-PINN,

$$\gamma(\xi) = \left[\cos(\mathbf{B}\xi), \sin(\mathbf{B}\xi)\right] \tag{20}$$

but the frequency matrix B is no longer fixed. Instead, it is periodically updated at predefined training iterations based on the intermediate training results. This adaptive update enables the network to progressively refine the spectral resolution, emphasizing frequency components that are underrepresented or poorly learned in earlier training stages. Conceptually, the adaptive strategy operates as:

1. Training is initiated using an initial frequency matrix $\mathbf{B}^{(0)}$, selected to provide a broad spectral coverage.
2. The network undergoes continuous training, with both the neural network weights and the frequency scaling parameter σ being optimized simultaneously through gradient descent algorithm to minimize the total loss.
3. The scalar frequency scale σ evolves continuously through gradient-based optimization, proportionally scaling all components of the fixed directional matrix $\mathbf{B}$ to adjust spectral coverage without discrete matrix updates.
4. The updated Fourier features are then used to continue training, allowing the network to focus on unresolved or emerging high-frequency components.

During training, the Gaussian scaling parameter σ is optimized through a mathematical reparameterization that enhances both the smoothness and stability of the optimization process. Specifically, we introduce an auxiliary parameter λ defined as:

$$\lambda = \log(\sigma_{\text{new}}) \tag{21}$$

This logarithmic transformation provides several benefits. By optimizing λ instead of σ directly, the model gains the ability to explore a wider range of scaling factors across iterations. More precisely, this reparameterization reduces the model's sensitivity to abrupt changes in the frequency scaling induced by the fixed projection matrix B. Consequently, even minor adjustments to λ by the optimizer enable the AF-PINN to efficiently explore a broad frequency spectrum while preventing numerical instability that could arise from extreme σ values. The updated scaling parameter σ is then recovered back through exponentiation:

$$\sigma = \exp(\lambda) \tag{22}$$

The procedure of defined network is represented in **Figure 3**. By adapting the Fourier features, the AF-PINN effectively mitigates spectral bias while avoiding the need for excessively large or arbitrarily chosen fixed frequency sets. This dynamic adjustment is particularly beneficial for nonlinear non-Fourier heat conduction problems, where temperature-dependent material properties introduce additional coupling and multiscale behavior that cannot be captured efficiently using static spectral embeddings.

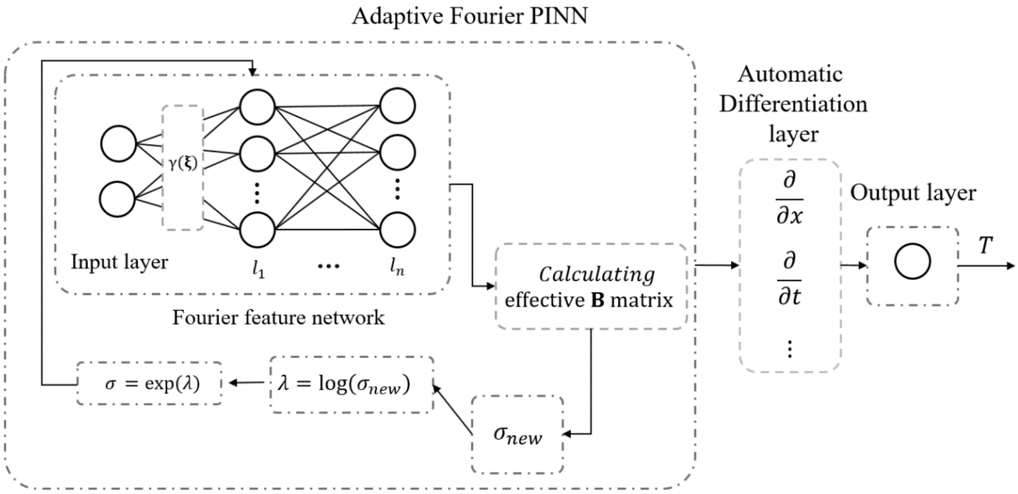

Figure 3: Schematic structure of AF-PINN

The AF-PINN thus provides a more flexible and robust framework for modeling thermal wave propagation in nonlinear hyperbolic heat conduction problems, forming the basis for the comparative analysis presented in the subsequent sections.

4. Results and Discussions

In this section, the performance of the proposed PINN-based frameworks is systematically evaluated against analytical and numerical reference solutions. Both linear and nonlinear non-Fourier heat conduction cases are examined to assess accuracy, convergence behavior, and robustness.

For temperature-independent thermal conductivity (γ = 0), the governing equation reduces to a linear hyperbolic form for which closed-form analytical solutions are available and are used here as benchmark references. When temperature-dependent thermal conductivity is considered ($\gamma \neq 0$), the governing equation becomes nonlinear and analytical solutions are unavailable. In this case, a high-resolution finite difference method (FDM) is employed as the reference solution.

The combined use of analytical solutions (for linear cases) and finite difference solutions (for nonlinear cases) ensures a comprehensive and consistent assessment of the proposed method across a wide range of physical scenarios relevant to non-Fourier heat transfer.

Figure 4 and **Figure 5** compare the temperature profiles predicted by the S-PINN and F-PINN against analytical reference solutions for linear (γ = 0) and nonlinear ($\gamma \neq 0$) non-Fourier heat conduction problems, respectively. Spatial distributions at a fixed time and temporal evolutions at a fixed spatial location are presented to assess both spatial and temporal learning behavior.

For the linear case (γ = 0) shown in **Figure 4**, both S-PINN and F-PINN demonstrate good agreement with the analytical solution. However, the S-PINN exhibits a consistently closer match in the spatial temperature profile, particularly near regions of higher curvature. This mismatch is attributed to the Fourier feature mapping, which transforms the input space with oscillatory components and mitigates the spectral bias inherent to standard fully connected networks.

The advantage of the F-PINN becomes more pronounced in the nonlinear case ($\gamma \neq 0$), where temperature-dependent material properties amplify high-frequency solution components as shown in **Figure 5**. While S-PINN still captures the overall trend of the solution, noticeable deviations from the reference profile appear in the spatial distribution, particularly around the peak temperature region. In contrast, the F-PINN maintains improved accuracy and better alignment with the reference solution. This observation highlights that nonlinear temperature-dependent material properties amplify high-frequency components in the solution, further exposing the limitations of standard PINNs and emphasizing the benefit of Fourier-based representations.

These results indicate that fixed Fourier-feature PINNs can outperform standard PINNs, particularly in nonlinear or multiscale regimes, provided that an appropriate spectral scale σ is selected. However, this apparent advantage is conditional: the performance of F-PINNs is highly sensitive to the choice of the Fourier bandwidth σ, which is problem-dependent and generally unknown a priori.

An inappropriate selection of σ can lead to under-representation or over-emphasis of certain frequency bands, resulting in degraded convergence or reduced solution accuracy. This sensitivity limits the robustness and general applicability of fixed Fourier-feature PINNs, particularly when dealing with varying physical parameters or strongly nonlinear regimes.

To overcome this limitation, an adaptive Fourier-feature PINN framework is introduced in the following sections. In this approach, the characteristic frequency content of the Fourier features is automatically adjusted during training, eliminating the need for manual tuning of σ and enhancing the stability and reliability of the model across different problem settings.

As discussed previously, the performance of the F-PINN architecture is highly sensitive to the choice of the Fourier feature bandwidth standard deviation σ. To systematically assess this sensitivity, the F-PINN model was trained using a range of initial bandwidth values ($\sigma_{init} \in \{0.5, 1, 2, 5\}$), while keeping all other network and training parameters unchanged.

Figure 6 presents the resulting spatial and temporal temperature profiles for the linear case (γ = 0). It is observed that moderate bandwidth values ($\sigma \approx$ 1 and 2) enable the F-PINN to accurately reproduce the numerical reference solution, capturing both the spatial peak and temporal evolution with high fidelity. In contrast, smaller bandwidths (σ = 0.5) lead to overly smooth predictions and overfit of spatial gradients. More critically, excessively large bandwidths (σ = 5) result in a complete breakdown of the solution, with the model failing to capture the underlying temperature dynamics in both space and time.

These results clearly demonstrate that although fixed Fourier features can significantly enhance model expressiveness, their effectiveness strongly depends on the appropriate selection of σ, which is not known as a priori and is highly problem dependent.

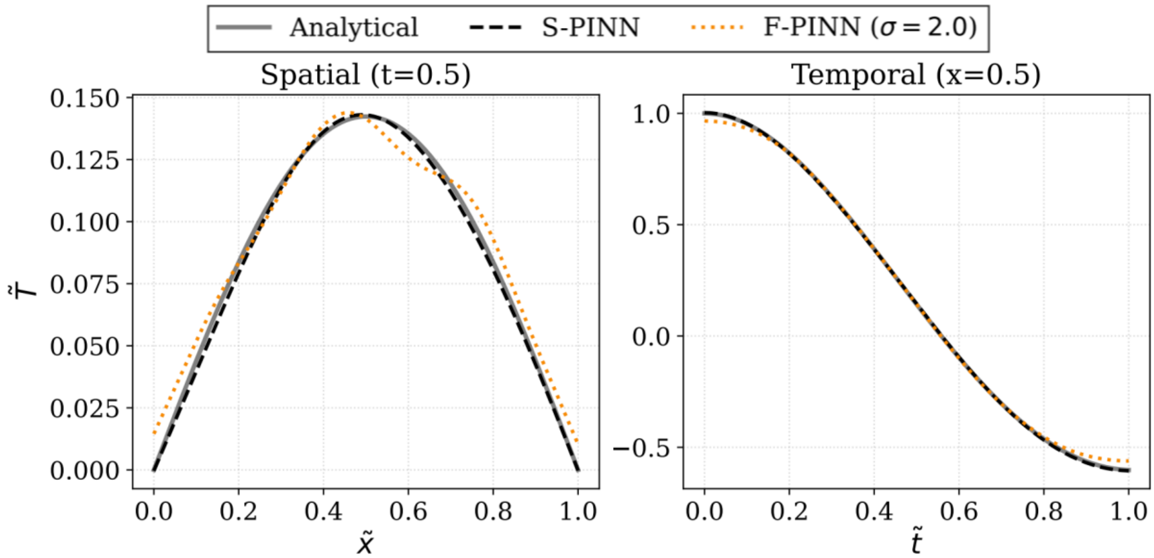

Figure 4: Comparison of spatial and temporal temperature profiles predicted by S-PINN and F-PINN (σ = 2.0) against the analytical solution for the linear non-Fourier heat conduction case (γ = 0.0).

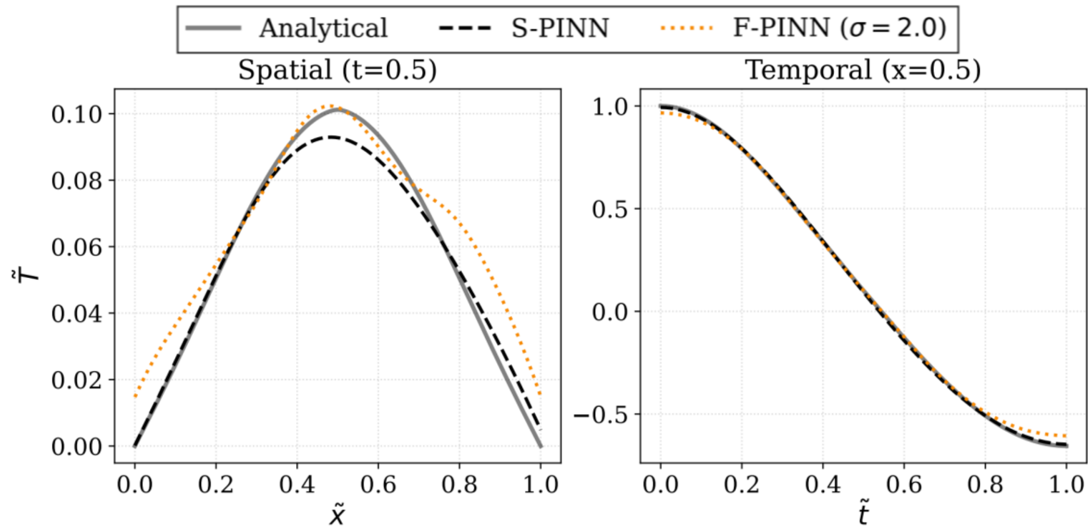

Figure 5: Comparison of spatial and temporal temperature profiles predicted by the S-PINN and fixed F-PINN (σ = 2.0) against the numerical reference solution for the nonlinear non-Fourier heat conduction case with temperature-dependent thermal conductivity (γ =0.2).

The influence of the Fourier feature bandwidth initialization, denoted by σ_{init} , was systematically investigated by training both F-PINNs and AF-PINNs over a wide range of initial scales i.e. $\sigma_{init} \in \{0.51, 2, 3, 4, 5\}$. In F-PINNs, the spectral content of the input mapping is fully determined at initialization, imposing a rigid inductive bias that constrains the network's ability to represent the solution across different frequency regimes. As demonstrated in the previous section, this rigidity leads to pronounced sensitivity to σ_{init} , particularly under nonlinear conditions.

In contrast, the proposed AF-PINN treats the global Gaussian scale σ as a learnable parameter, decoupled from the directional matrix $\mathbf{B}$. This formulation enables dynamic adjustment of the spectral bandwidth during training, allowing the network to progressively align its frequency representation with the dominant physical features of the solution.

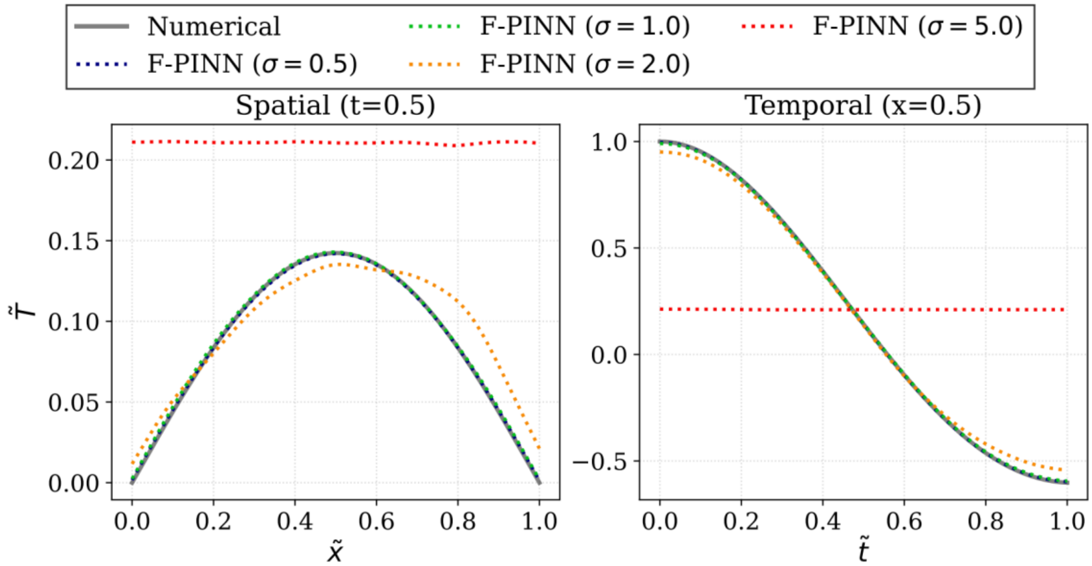

Figure 6: Sensitivity of F-PINN predictions to the bandwidth parameter σ for the linear case (γ = 0.0). Spatial and temporal temperature profiles are shown for different σ initializations, highlighting over-smoothing at small σ and instability at large σ.

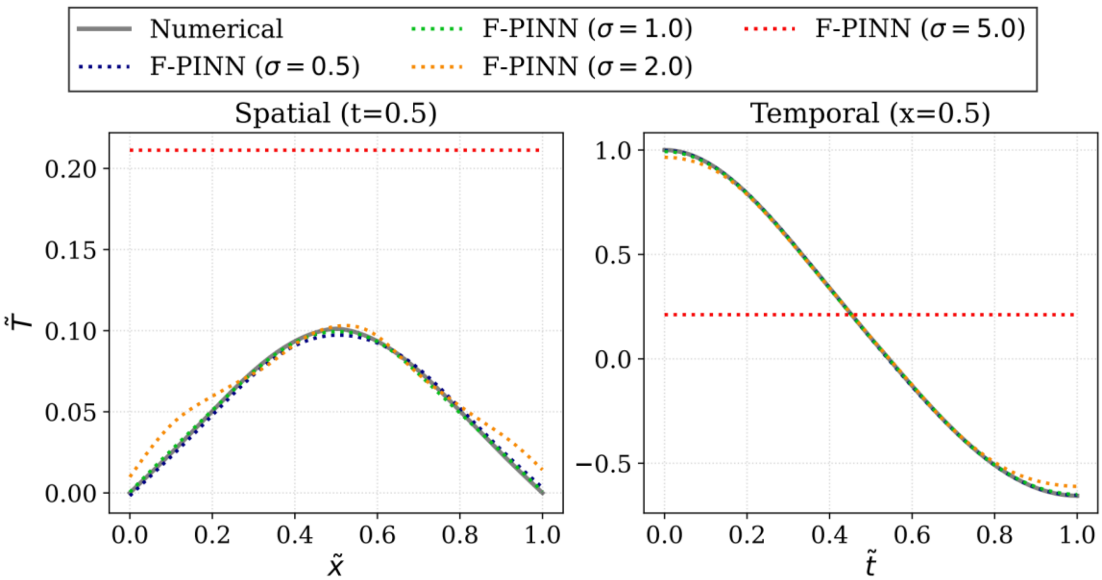

Figure 7:Sensitivity of F- PINN predictions to the bandwidth parameter σ for the nonlinear case (γ = 0.2). Large σ values lead to severe degradation of solution accuracy due to excessive high-frequency bias.

Figure 8 and **Figure 10** show that, regardless of initialization, the adaptive bandwidth converges toward a narrow range, indicating the presence of a stable basin of attraction driven by physics-informed loss.

To further assess the stability of the adaptive process, the total loss function comprising the PDE residual, boundary condition, and initial condition losses was monitored throughout training, as shown in **Figure 9** and **Figure 11**. The results reveal a clear correlation between the stabilization of the Gaussian scale and the sharp reduction of the total loss. Importantly, even for highly suboptimal initializations (e.g., σ_{init} =5), the AF-PINN successfully escapes poor spectral configurations and converges to a low-error solution, whereas the corresponding fixed Fourier models fail to do so.

The practical implications of this self-tuning behavior are highlighted in **Figure 12** and **Figure 13**, which compare spatial and temporal temperature profiles obtained using different initial scale guesses. For both γ =0 and γ =0.2, the AF-PINN predictions collapse onto a single, consistent solution that closely matches the analytical reference, regardless of the initial bandwidth. This insensitivity to σ_{init} stands in stark contrast to the fixed Fourier PINN results discussed earlier, where solution accuracy varied dramatically with the chosen scale.

Overall, these results demonstrate that AF-PINN transforms the Fourier bandwidth from a static, manually tuned hyperparameter into a dynamic, physics-driven variable learned during training.

As demonstrated in **Figure 12** and **Figure 13**, a strong correlation exists between the evolution of the Gaussian scale parameter and the minimization of the total residual loss within the AF-PINN framework. Effective reduction of the physics-informed loss is contingent upon proper calibration of the Fourier bandwidth. Since the optimal value of σ is inherently problem-dependent rather than universal, its accurate identification here is achieved through the adaptive learning mechanisms essential for ensuring stable and robust convergence.

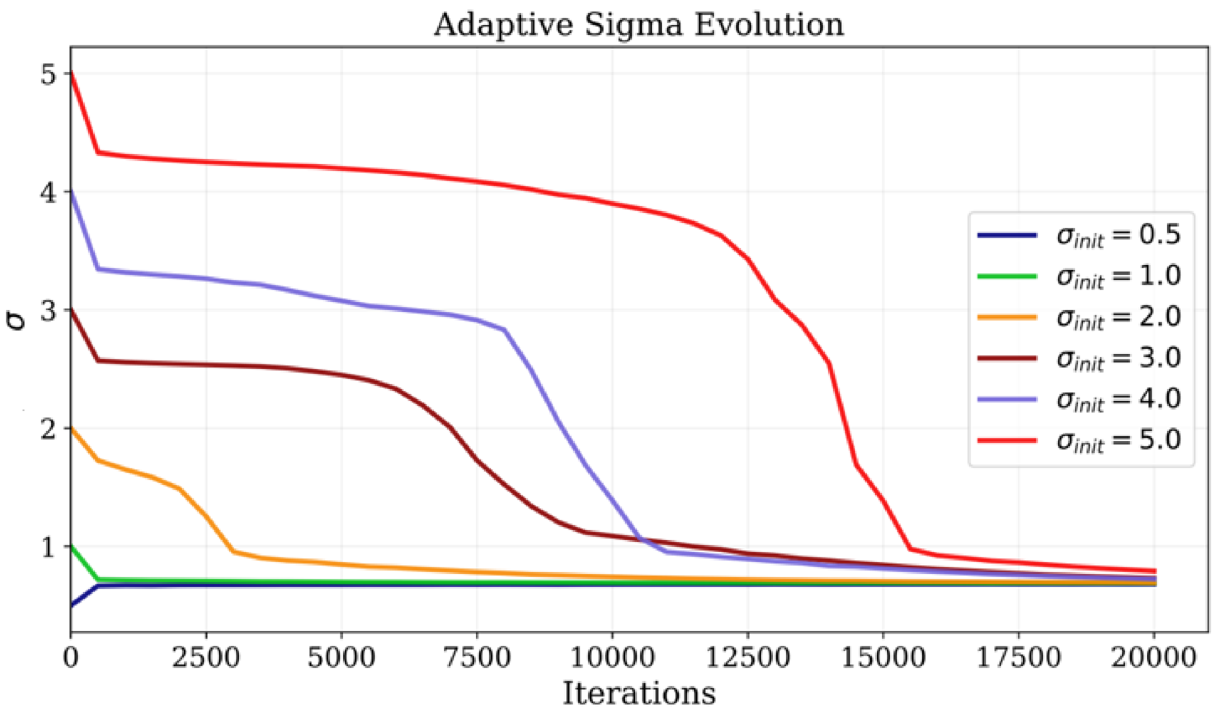

Figure 8: Evolution of the learnable Gaussian bandwidth parameter σ during AF-PINN training for the linear case (γ = 0.0) under different initial bandwidth guesses, demonstrating convergence toward a stable spectral scale.

Due to stochastic effects arising from random initialization, collocation sampling, and optimization, exact determinism cannot be guaranteed. To maintain a controlled experimental setup, the random number generators of NumPy, PyTorch, and CUDA were explicitly synchronized. Performance metrics were then evaluated statistically across these repeated trials. This Monte Carlo–style analysis aims to verify that the AF-PINN consistently converges to the same solution with minimal variance, thereby demonstrating stable and reproducible behavior.

The convergence trajectories of both the adaptive Gaussian scale and the total loss are presented in **Figure 14** for the linear case (γ = 0). In these plots, the shaded regions represent the envelope defined by the minimum and maximum values observed across all seeds, while the solid curves denote the median trajectory at each training iteration. Despite differences in initialization, the adaptive scale converges toward a narrow range, accompanied by consistent loss decay, indicating that the learning dynamics are largely insensitive to stochastic perturbations. To balance computational cost and statistical relevance, this analysis was conducted for the representative set of initial scales $\sigma_{init} \in \{0.5, 1, 2, 5\}$.

A similar trend is observed for the nonlinear case (γ = 0.2), as shown in **Figure 15**. Regardless of the initial bandwidth including highly suboptimal values such as σ_{init} =5, the adaptive mechanism rapidly adjusts the spectral scale and drives the total loss to the same order of magnitude achieved by runs initialized near the optimal range. This behavior confirms that the AF-PINN's ability to recover the relevant spectral content is not a consequence of favorable random initialization, but rather an intrinsic property of the adaptive optimization landscape.

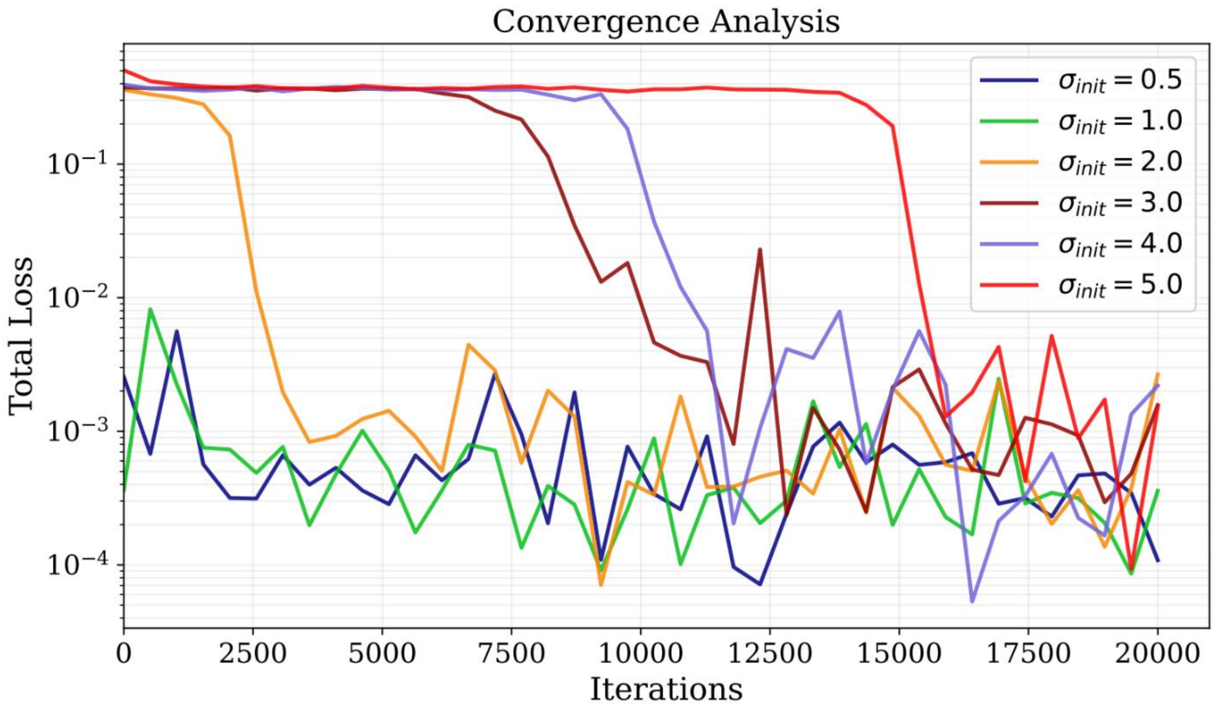

Figure 9: Convergence of the total physics-informed loss during AF-PINN training for the linear case (γ = 0.0), showing strong correlation between loss decay and stabilization of the adaptive bandwidth.

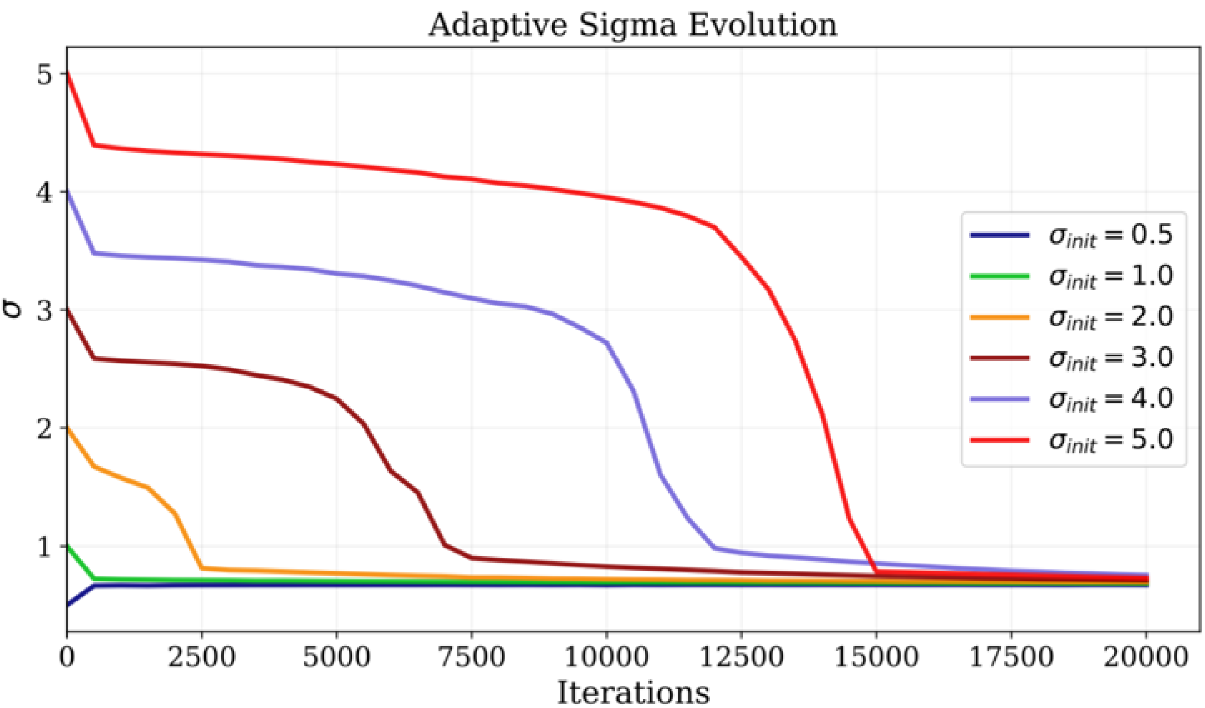

Figure 10: Evolution of the learnable Gaussian bandwidth parameter σ during AF-PINN training for the nonlinear case (γ = 0.2) under different initial bandwidth guesses, illustrating robust convergence despite adverse initialization.

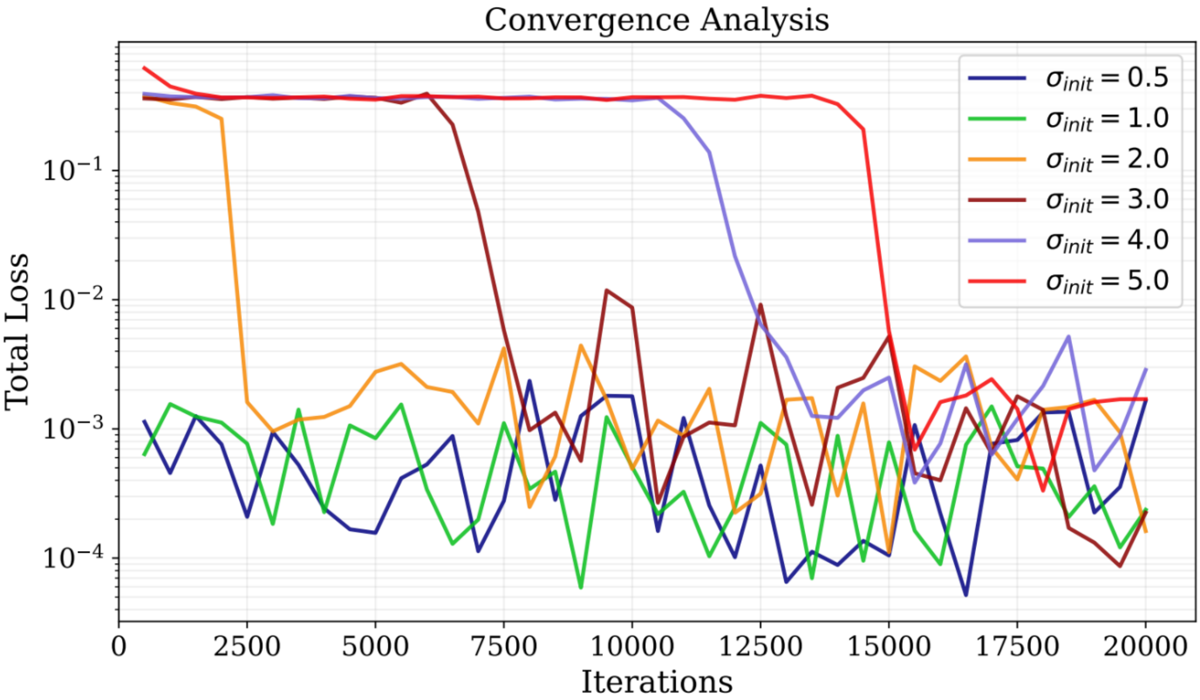

Figure 11: Convergence of the total physics-informed loss during AF-PINN training for the nonlinear case (γ = 0.2), confirming stable optimization behavior across different initial spectral scales.

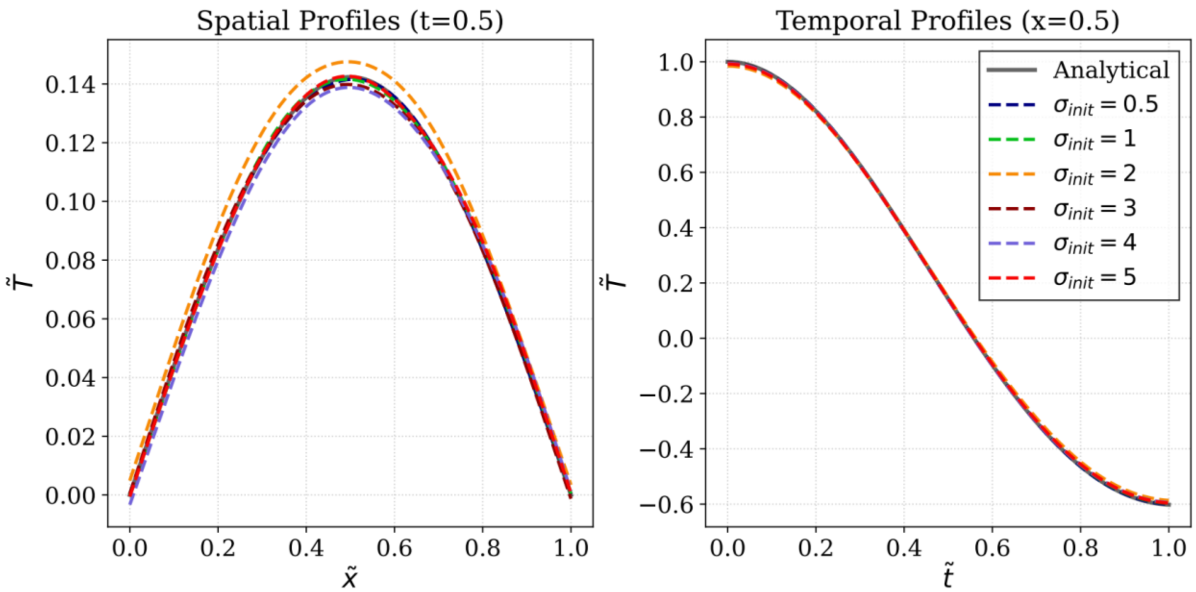

Figure 12: Spatial and temporal temperature profiles predicted by the AF-PINN for the linear case (γ = 0.0) using different initial bandwidth values, demonstrating insensitivity of the final solution to σ initialization.

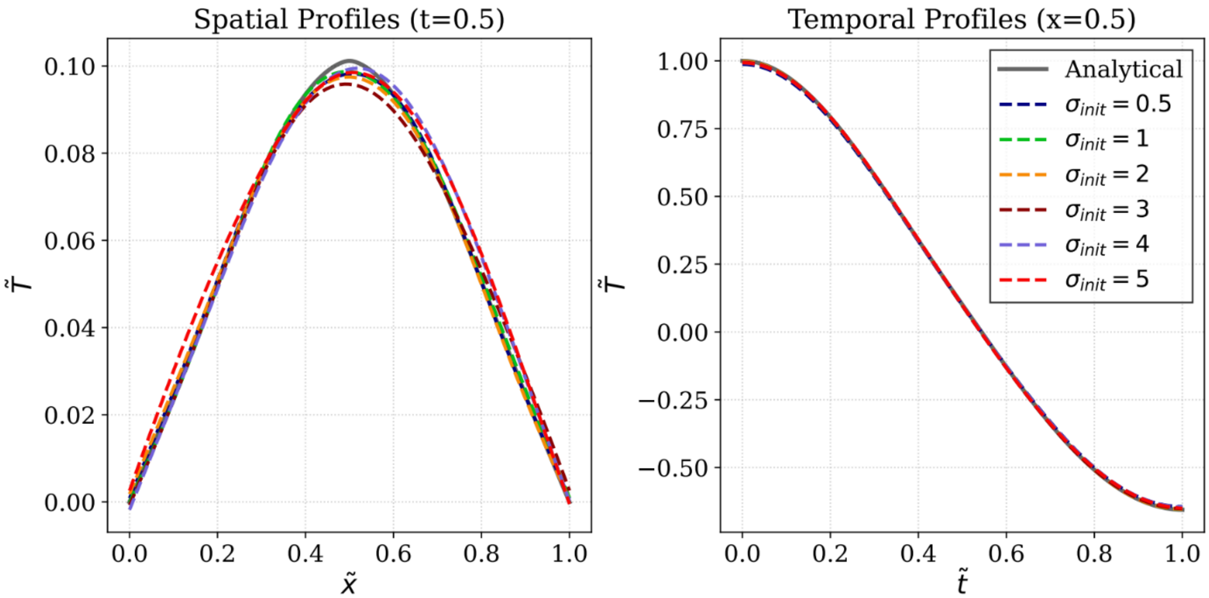

Figure 13: Spatial and temporal temperature profiles predicted by the AF-PINN for the nonlinear case (γ = 0.2) using different initial bandwidth values, confirming robust recovery of the physical solution.

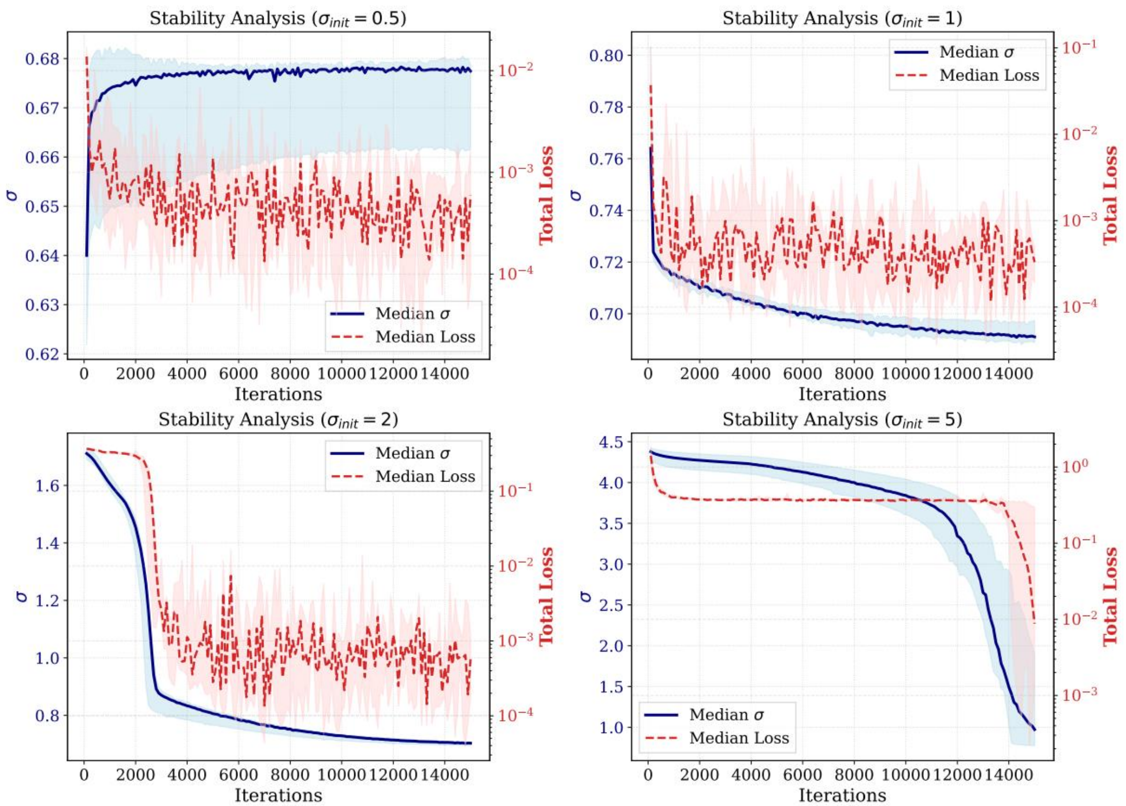

Figure 14: Statistical convergence behavior of the AF-PINN for the linear case (γ = 0.0) across multiple random initializations. Shaded regions indicate the minimum–maximum envelope, and solid lines represent the median trajectory.

While the convergence behavior of the loss function and the adaptive bandwidth provide valuable insight into the optimization dynamics, the most critical measure for practical applicability is the reliability of the predicted temperature field itself. To quantify the impact of initialization-induced stochasticity on the final solution, temperature profiles were evaluated across the full ensemble of independent training runs.

The resulting spatial and temporal temperature distributions, evaluated at representative mid-domain locations ($\tilde{x}$=0.5 and $\tilde{t}$ =0.5), are presented in **Figure 16** and **Figure 17**. Consistent with the statistical visualization used previously, the solid-colored curves denote the median prediction across all random seeds, while the shaded bands represent the uncertainty envelope, defined by the minimum and maximum predicted values. The analytical (for the linear case) and numerical (for the nonlinear case) reference solutions are superimposed to assess predictive accuracy.

For both linear and nonlinear cases, the AF-PINN predictions exhibit an exceptionally narrow uncertainty envelope, with the median solution almost indistinguishable from the corresponding reference profile. The negligible spread among realizations confirms that the adaptive mechanism effectively suppresses variability arising from random initialization and stochastic optimization effects. Importantly, this statistical consistency is maintained despite the use of a fixed initial bandwidth (σ_{init} =2), further demonstrating that the final solution is governed by the physics-informed learning process rather than the choice of initialization.

These results provide strong evidence that the proposed AF-PINN framework delivers not only stable convergence at the optimization level, but also highly reliable and reproducible field predictions, satisfying a key requirement for physics-based surrogate modeling of non-Fourier heat transfer phenomena.

To provide a rigorous quantitative assessment of model performance, the predictive accuracy is evaluated using the relative L^2 error norm defined over the entire spatiotemporal domain (x,t). While physics-informed neural networks often satisfy boundary and initial conditions with high precision, this localized accuracy does not necessarily imply correct solution behavior in the interior of the domain. Consequently, a global metric is required to prevent misinterpretation of the model's true fidelity. The relative L^2 error is calculated as follows:

$$L^2 = \frac{\sqrt{\sum_{j=1}^{N_t}\sum_{i=1}^{N_x}\left(T_{\text{PINN}}(x_i,t_j) - T_{\text{FDM}}(x_i,t_j)\right)^2}}{\sqrt{\sum_{j=1}^{N_t}\sum_{i=1}^{N_x}T_{\text{FDM}}(x_i,t_j)^2}} \tag{23}$$

where T_{PINN} represents the model prediction and T_{FDM} denotes the high-resolution numerical reference solution. To systematically quantify the stability of the solution method against initialization stochasticity, the experiment was conducted using an ensemble of independent training runs initialized with distinct random seeds.

The statistical distribution of the relative L^2 error and the final training loss for the S-PINN, F-PINN, and AF-PINN are presented in the boxplots below. These metrics are reported across varying initialization scales.

For the linear case (γ =0), the results reveal a fundamental trade-off inherent to fixed Fourier feature mappings. As shown in **Figure 18** and **Figure 19**, the F-PINN achieves excellent accuracy when initialized at an optimal bandwidth (σ =1.0), outperforming the S-PINN baseline in terms of both median L^2 error and final loss. However, this performance is highly volatile. At larger bandwidths (σ =5.0), the error variance increases dramatically and the mean L^2 error deteriorates by orders of magnitude, as evidenced by the pronounced outliers in the boxplots and the dark blue region in the heatmap.

In contrast, the AF-PINN demonstrates remarkable robustness to the initial bandwidth selection. Across all tested values of σ, the adaptive model consistently converges to the low-error regime, achieving accuracy comparable to the optimally tuned F-PINN without requiring manual hyperparameter selection. Both the boxplots and the heatmap confirm that the AF-PINN maintains low mean error and minimal variance, indicating stable and repeatable convergence behavior.

A similar trend is observed for the nonlinear case (γ =0.2), as illustrated in **Figure 20** and **Figure 21**, although the contrast between the models becomes even more pronounced. The F-PINN again exhibits strong sensitivity to the choice of σ, with performance degrading rapidly for non-optimal bandwidths. In particular, large initial scales lead to persistent high errors and elevated training loss, reflecting the difficulty of manually selecting an appropriate spectral scale in nonlinear regimes.

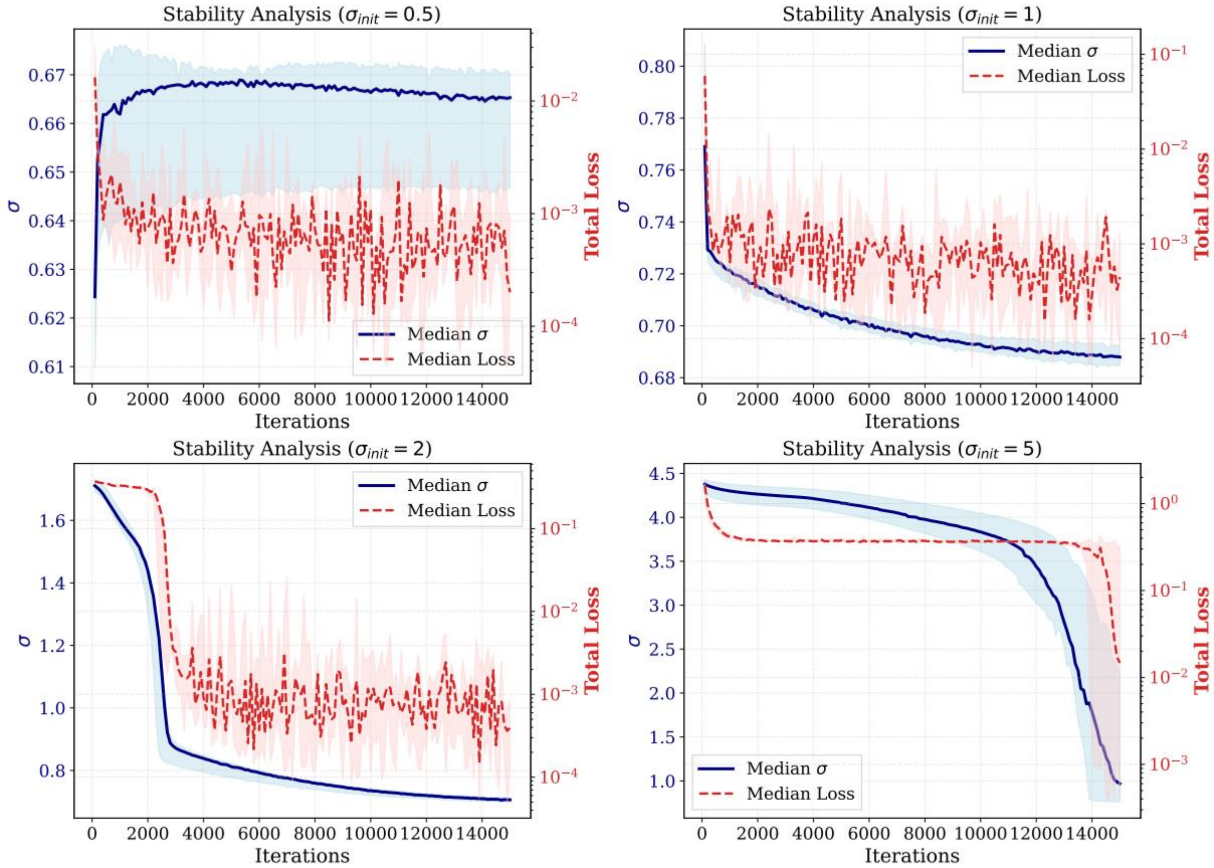

Figure 15: Statistical convergence behavior of the AF-PINN for the nonlinear case (γ = 0.2) across multiple random initializations, demonstrating reproducible loss decay and adaptive bandwidth stabilization.

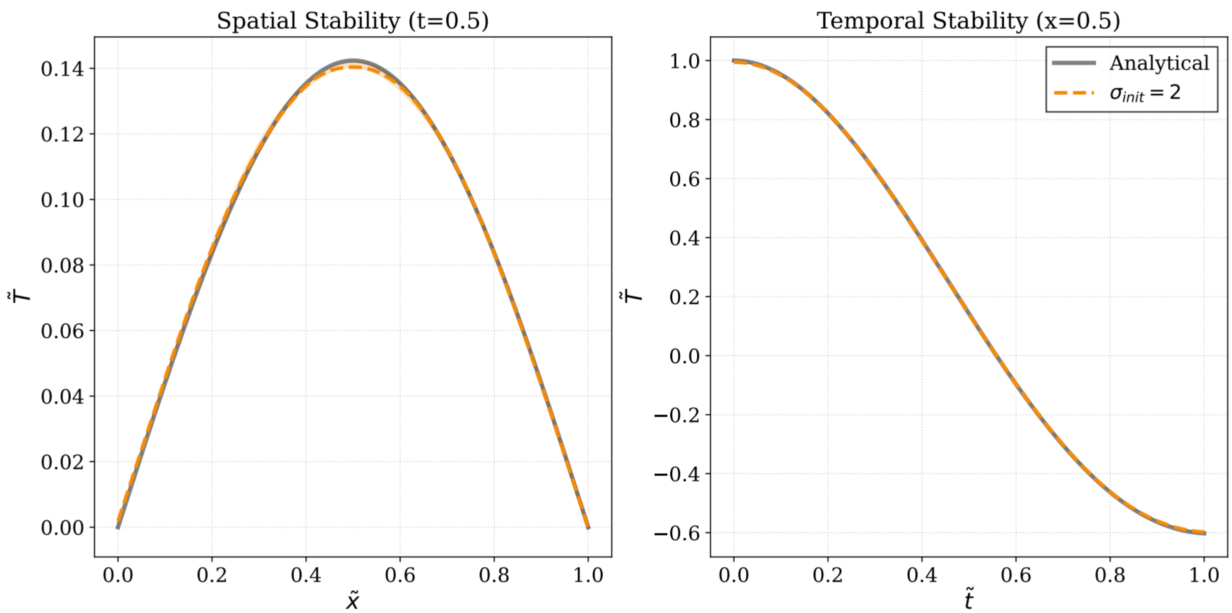

Figure 16: Statistical consistency of AF-PINN spatial and temporal temperature predictions for the linear case (γ = 0.0) evaluated at representative mid-domain locations. Shaded regions indicate prediction variability across random seeds.

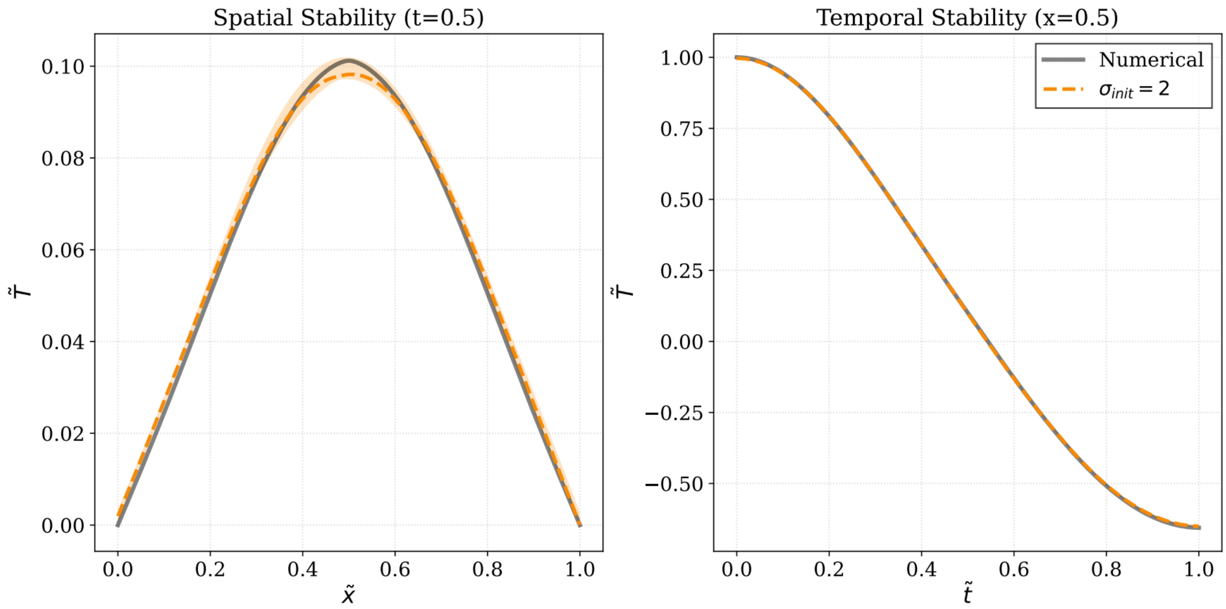

Figure 17: Statistical consistency of AF-PINN spatial and temporal temperature predictions for the nonlinear case (γ = 0.2), illustrating minimal uncertainty and close agreement with the numerical reference solution.

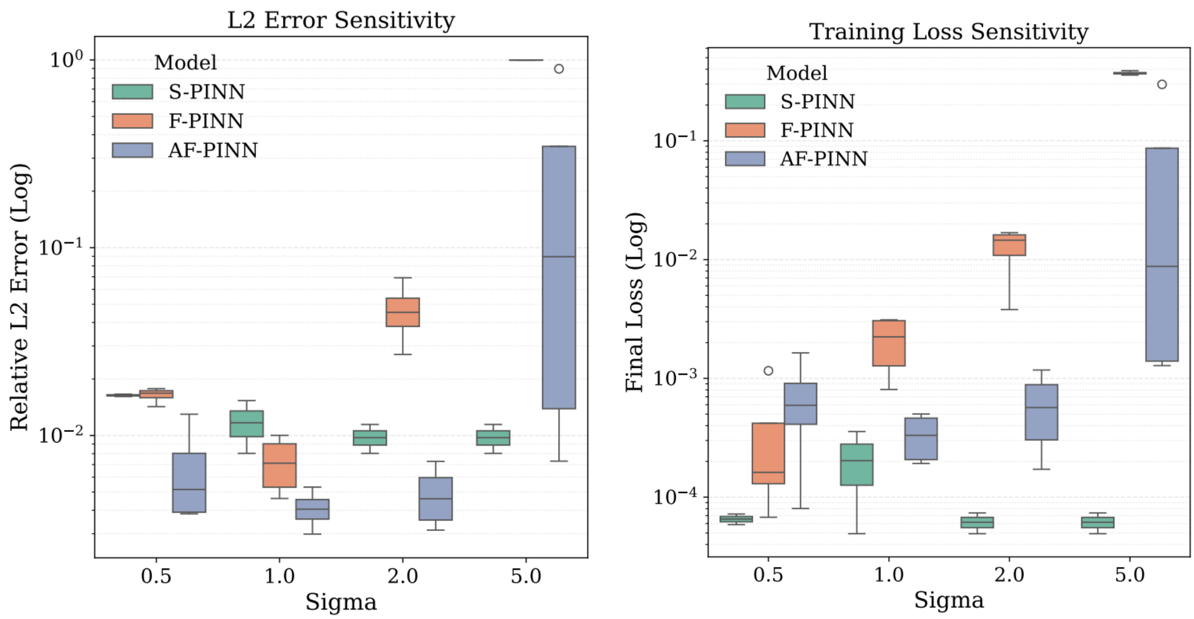

Figure 18: Boxplot comparison of relative L² error and final training loss for S-PINN, F-PINN, and AF-PINN models under different bandwidth initializations for the linear case (γ = 0.0).

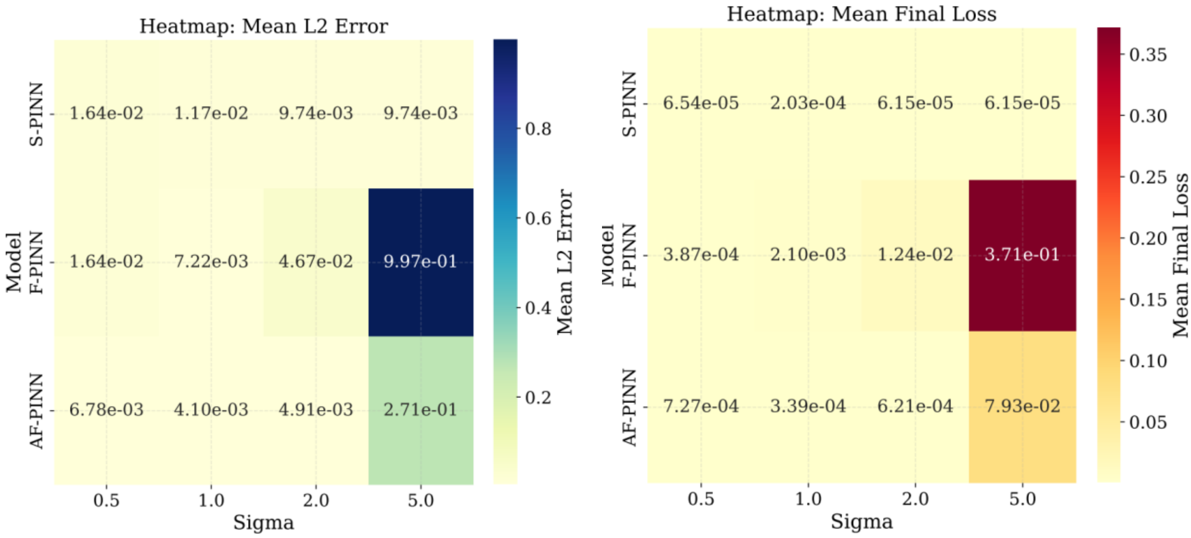

Figure 19: Heatmap visualization of mean relative L^2 error and total loss for S-PINN, F-PINN, and AF-PINN models across different bandwidth initializations for the linear case (γ = 0.0).

By comparison, the AF-PINN retains its robustness under nonlinear conditions. Regardless of the initial bandwidth, the adaptive framework consistently converges to a stable low-error solution with limited dispersion across random seeds. This behavior confirms that the adaptive learning of the Fourier bandwidth is not merely beneficial in linear settings but remains effective when temperature-dependent material properties introduce additional nonlinearity and spectral complexity.

This robustness becomes particularly critical in the nonlinear regime (γ =0.2). As shown in **Figure 20**, the fixed F-PINN exhibits severe performance degradation when initialized with non-optimal bandwidths, with several realizations failing to converge to a meaningful solution. These failures indicate that inappropriate high-frequency initialization biases are especially detrimental when coupled with nonlinear temperature-dependent dynamics, where the solution spectrum evolves during training.

In contrast, the AF-PINN consistently maintains low prediction error across all tested initializations, achieving a mean relative L^2 error on the order of 6.3×10^{-3} even under highly unfavorable initial conditions. By dynamically adapting its spectral scale during training, the AF-PINN effectively mitigates spectral bias and prevents convergence to spurious solutions, resulting in a model that is both accurate and algorithmically robust.

The improved robustness of the AF-PINN is achieved at the expense of a modest increase in computational cost. As shown in **Figure 22**, the adaptive model requires approximately 2.8 minutes of training time, compared to 2.5 minutes for the fixed F-PINN and 1.8 minutes for the S-PINN. This additional cost is attributable to the extended training duration required to reliably capture the adaptive bandwidth dynamics. All simulations were performed on an NVIDIA A100 GPU, utilizing a Colab subscription service. Nevertheless, given the substantial gains in stability, accuracy, and elimination of manual hyperparameter tuning, this overhead is relatively small and justified for nonlinear non-Fourier heat transfer problems.

To further understand the behavior of the adaptive framework under adversarial spectral initialization, the optimization dynamics of the AF-PINN are examined in detail. While the AF-PINN significantly outperforms fixed Fourier feature baselines, the nonlinear case initialized at an extreme bandwidth (σ_{init} =5.0) reveals the intrinsic difficulty of the underlying optimization landscape. As observed in **Figure 20** and further elucidated by the convergence trajectories, this regime is characterized by highly non-smooth dynamics. The fixed F-PINN completely collapses into a high-error state with substantial variance, failing to recover the physically meaningful solution.

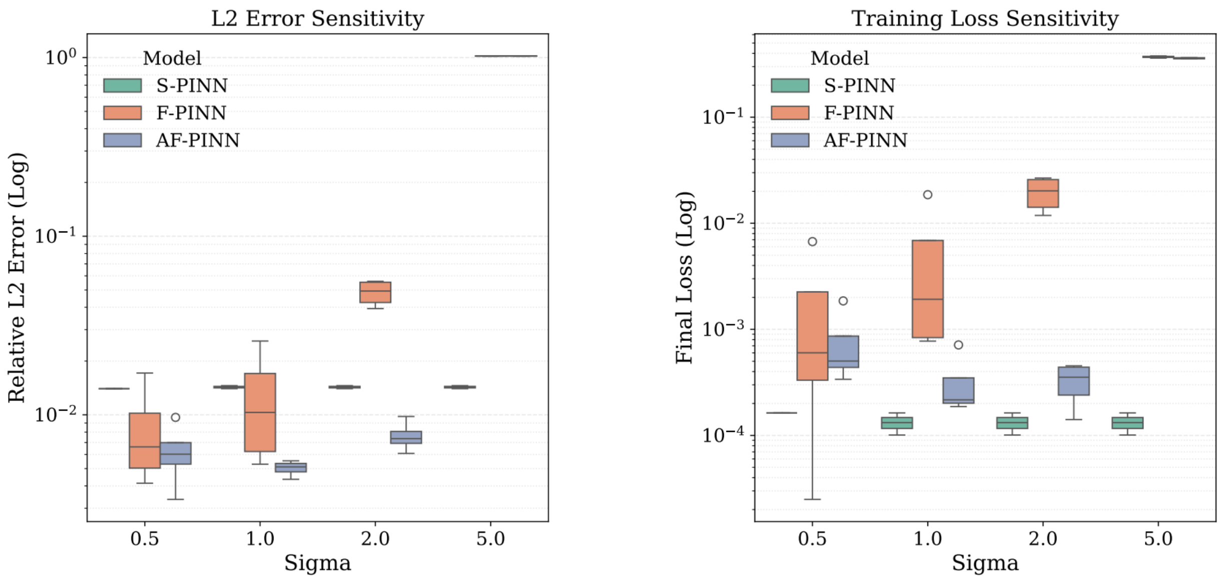

Figure 20: Boxplot comparison of relative L² error and training loss for S-PINN, F-PINN, and AF-PINN models under different bandwidth initializations for the nonlinear case (γ = 0.2), highlighting severe instability of fixed Fourier features.

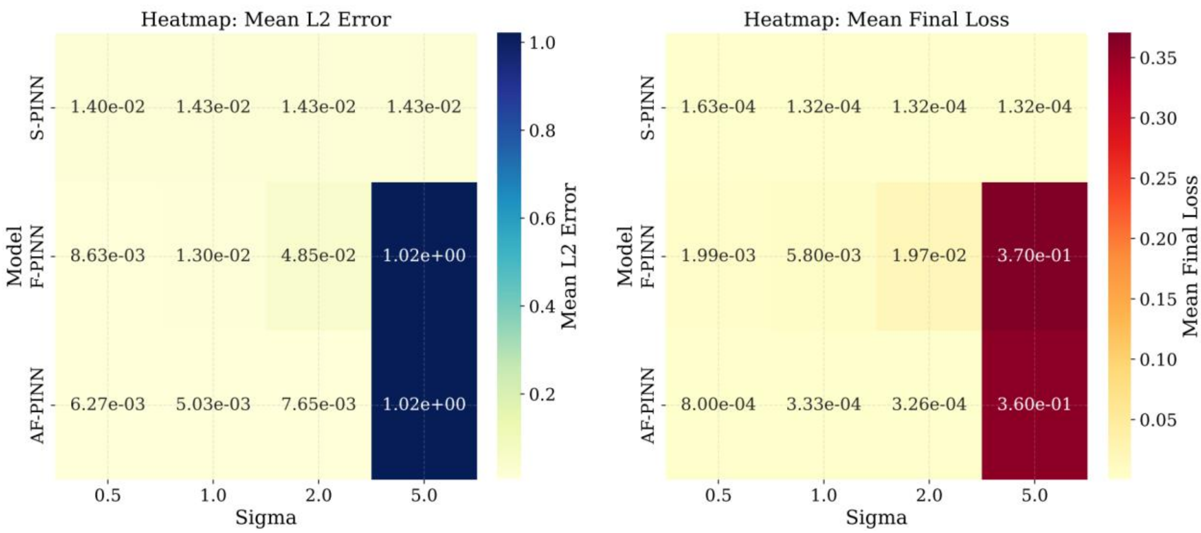

Figure 21: Heatmap visualization of mean relative L² error and total loss for S-PINN, F-PINN, and AF-PINN models across different bandwidth initializations for the nonlinear case (γ = 0.2).

Although the AF-PINN remains capable of eventual recovery, this adversarial initialization represents its most challenging operating regime. Compared to the smooth and monotonic convergence observed for moderate initializations (e.g., σ =1.0), the σ_{init} =5.0 case exhibits delayed convergence and elevated transient variance. In this setting, the adaptive model must aggressively drive the spectral scale away from a high-frequency local minimum before meaningful physics can be learned by the spatial weights. This behavior highlights that adaptivity alone does not guarantee efficient convergence; rather, the mechanism governing how the spectral scale is updated plays a decisive role in enabling recovery.

The analysis of the adversarial initialization demonstrates that treating the Gaussian bandwidth as a learnable parameter is a necessary but not sufficient condition for robust optimization. The learning dynamics of the spectral scale σ differ fundamentally from those of the network weights $\mathbf{W}$ and biases $\mathbf{b}$. While standard PINN training typically employs a single global learning rate, this strategy is suboptimal in the AF-PINN framework.

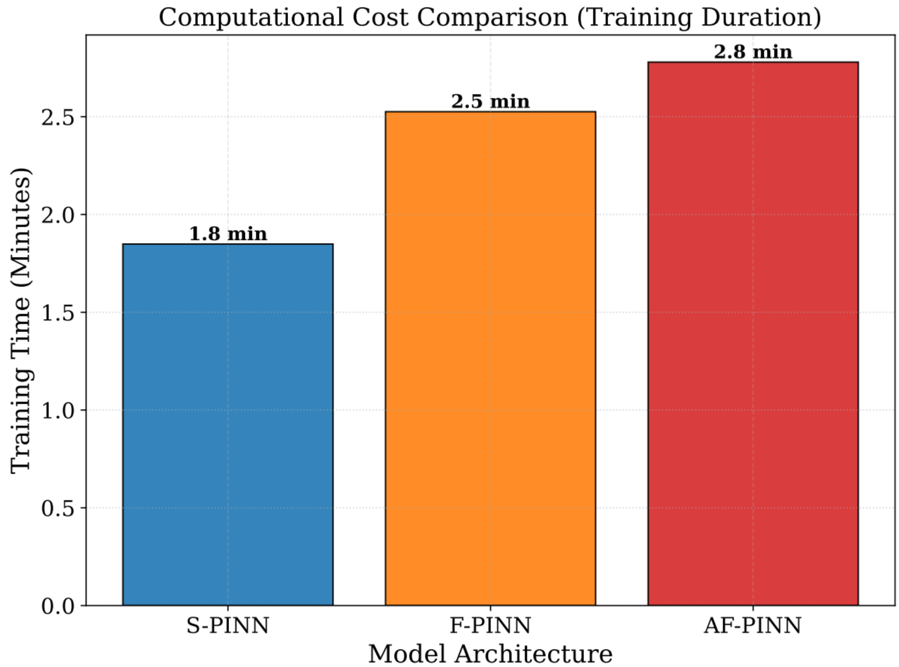

Figure 22: Comparison of total training time required by S-PINN, F-PINN, and AF-PINN models for the nonlinear case (γ = 0.2), illustrating the modest computational overhead introduced by adaptive spectral learning.

The spectral scale σ functions as a global frequency modulator. If its learning rate is too small, the model remains trapped in the initial spectral bias long enough for the spatial weights to overfit incorrect frequency content. Conversely, a sufficiently large learning rate enables rapid traversal of the frequency space, allowing the network to identify the physically relevant spectral regime before fine-scale fitting occurs.

To address this kinetic mismatch, a dual learning-rate optimization strategy is adopted, in which the bandwidth parameter is updated independently of the remaining network parameters:

$$\begin{aligned} \boldsymbol{\theta}_{t+1} &= \boldsymbol{\theta}_t - \eta_{\text{net}} \nabla_{\boldsymbol{\theta}} \mathcal{L}, \qquad \boldsymbol{\theta} \in \{\mathbf{W}, \mathbf{b}\}, \\ \sigma_{t+1} &= \sigma_t - \eta_\sigma \nabla_\sigma \mathcal{L}. \end{aligned} \tag{24}$$

This formulation allows the spectral scale to act as a coarse-tuning variable, rapidly positioning the network within the correct basin of attraction, while the weights and biases perform subsequent fine-scale refinement of the solution.

Figure 23 illustrates the evolution of the adaptive bandwidth and the corresponding loss convergence for different choices of the bandwidth learning rate η_σ, under the adversarial initialization σ_{init} =5.0. When η_σ is small, the scale parameter decays too slowly, prolonging the high-frequency bias and delaying convergence. In contrast, assigning a larger learning rate enables rapid correction of the spectral scale, leading to earlier stabilization of the loss and faster recovery of physically consistent dynamics.

This trade-off is quantified in **Figure 24**, which compares the final relative L^2 error against the total training time for different values of η_σ. An intermediate-to-large learning rate (η_σ =0.1) yields the best balance between accuracy and computational cost, reducing the error by more than an order of magnitude without a significant increase in runtime.

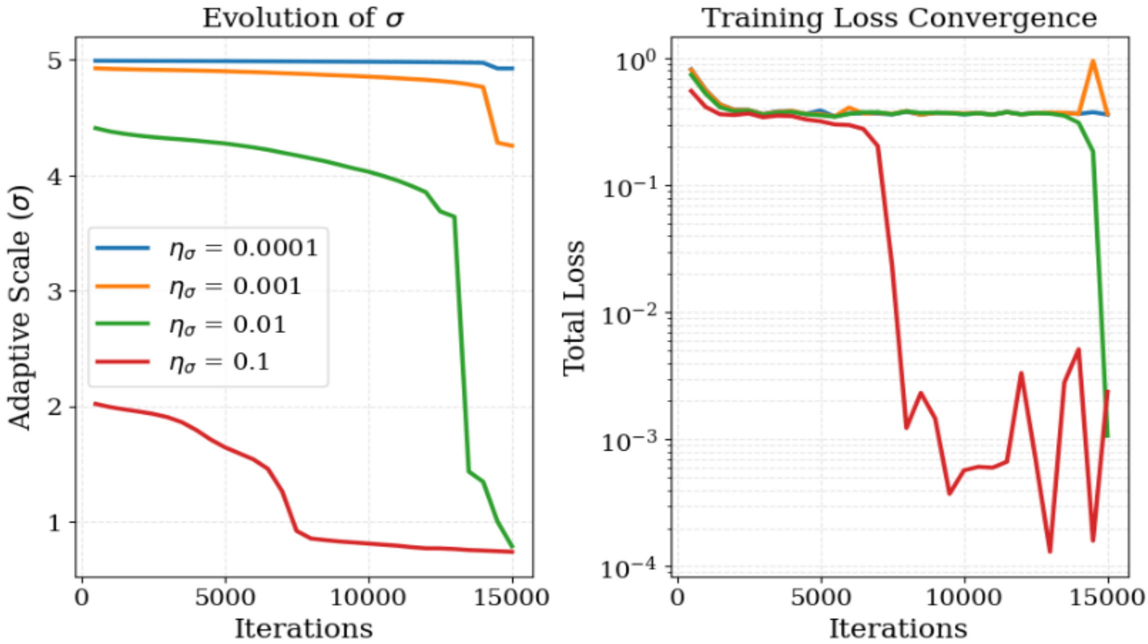

Figure 23: Evolution of the adaptive bandwidth parameter σ and corresponding loss convergence for the AF-PINN initialized at an adversarial spectral scale (σ_{init} = 5.0), under different bandwidth learning rates.

The resulting temperature profiles, shown in **Figure 25**, further confirm this behavior. For sufficiently large η_σ, the AF-PINN recovers both spatial and temporal temperature distributions that closely match the numerical reference, even when initialized far from the optimal spectral scale. Conversely, inadequate learning rates lead to persistent distortion in the spatial profile, indicating incomplete correction of the spectral bias.

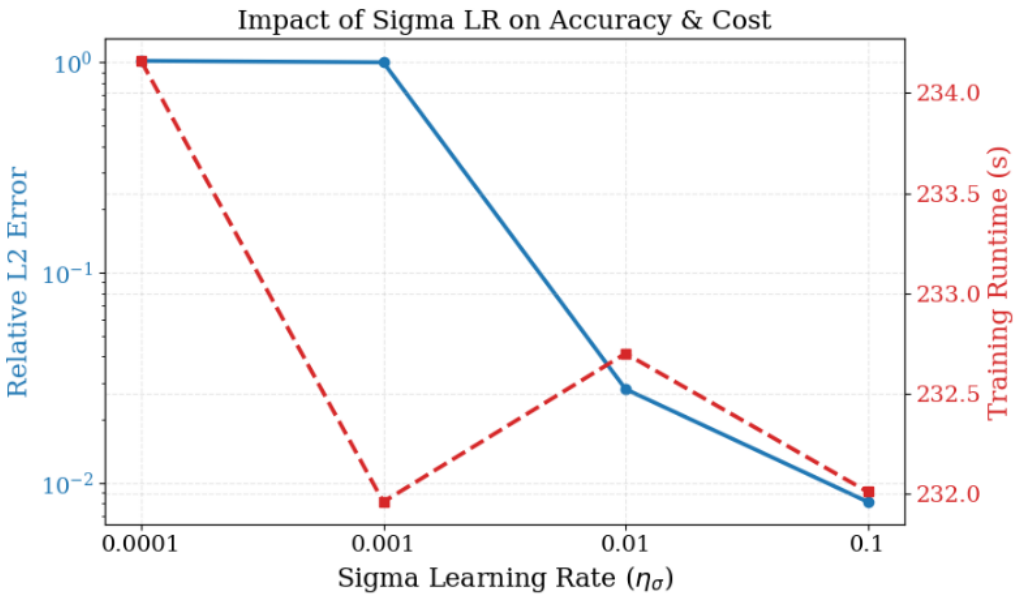

Figure 24: Trade-off between final relative L² error and computational training time for the AF-PINN under different bandwidth learning rates, highlighting the optimal balance between accuracy and efficiency.

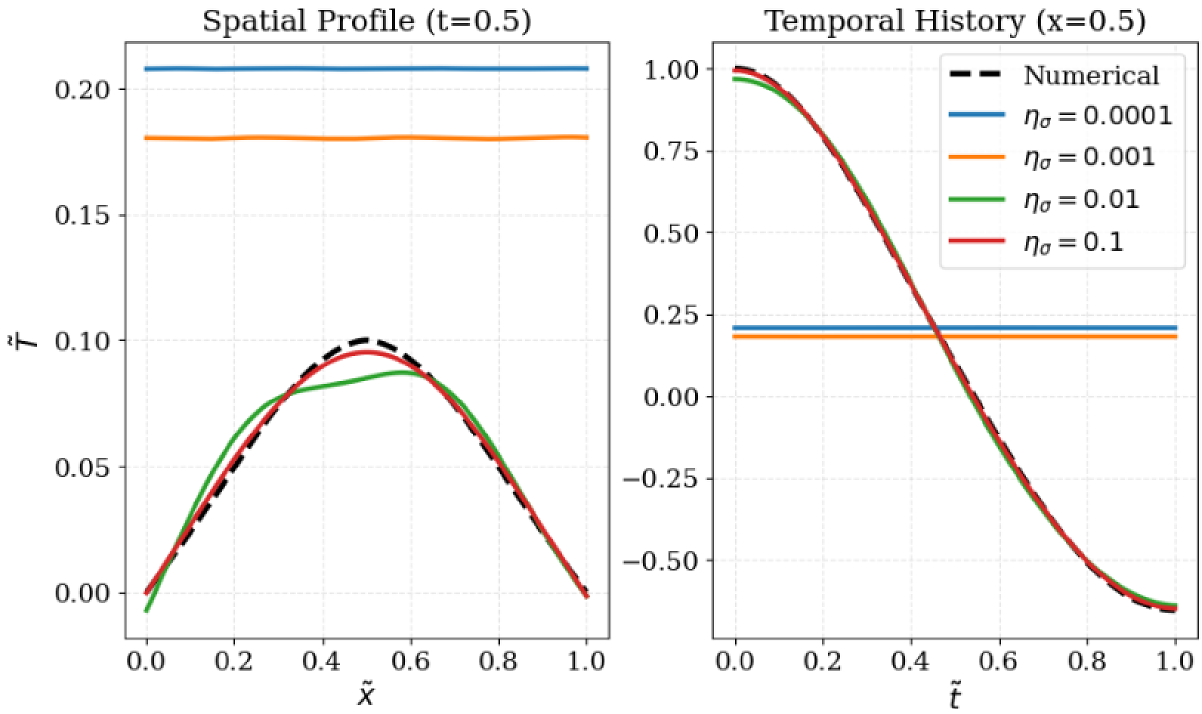

Figure 25: Final spatial and temporal temperature profiles predicted by the AF-PINN for different bandwidth learning rates under adversarial initialization (σ_{init} = 5.0), demonstrating recovery of the physical solution with appropriate optimization settings.

5. Conclusions

This study presented a comprehensive physics-informed neural network framework for solving the nonlinear CV non-Fourier heat conduction equation with temperature-dependent thermal conductivity. Three PINN architectures were systematically investigated: a standard PINN, a fixed Fourier Feature PINN, and a novel Adaptive Fourier Feature PINN. Their performance was evaluated in both linear and nonlinear regimes using analytical and high-resolution numerical reference solutions.

The results demonstrated that standard PINNs struggle to accurately capture the wave-like and multiscale characteristics of non-Fourier heat transfer, particularly in the presence of temperature-dependent material properties. This limitation was attributed to the inherent spectral bias of conventional neural networks, which favors low-frequency solution components. Introducing fixed Fourier feature mappings significantly improved solution accuracy by enhancing the representation of high-frequency content. However, the effectiveness of F-PINNs was shown to be highly sensitive to the choice of the Fourier bandwidth parameter, with performance degrading severely for non-optimal initialization values, especially in nonlinear regimes.

To overcome this limitation, an adaptive Fourier feature strategy was proposed, in which the Gaussian spectral bandwidth is treated as a learnable parameter and updated dynamically during training. The AF-PINN consistently demonstrated robust convergence across a wide range of initial bandwidths, eliminating the need for manual tuning. Statistical analyses based on multiple random initializations confirmed that the adaptive framework yields stable and reproducible solutions with minimal variance in both linear and nonlinear cases. Moreover, global relative L^2error metrics showed that the AF-PINN achieves accuracy comparable to, or exceeding, that of optimally tuned fixed F-PINNs, while maintaining significantly greater robustness.

A detailed investigation of the optimization dynamics further revealed that robust adaptivity requires not only a learnable spectral parameter but also an appropriate optimization strategy. By decoupling the learning rates of the spectral scale and the network weights, the AF-PINN was able to recover from adversarial high-frequency initializations that caused fixed Fourier models to fail. This dual learning-rate formulation enabled rapid correction of spectral bias and reliable convergence to physically meaningful solutions, at the cost of only a modest increase in computational time.

Overall, the findings demonstrate that AF-PINNs provide a powerful and reliable framework for modeling nonlinear non-Fourier heat transfer phenomena. By transforming the Fourier bandwidth from a static hyperparameter into a physics-driven, self-regulating variable, the proposed approach significantly enhances accuracy, stability, and generalizability. Beyond non-Fourier heat conduction, the methodology and insights presented in this work are directly applicable to a broader class of hyperbolic and multiscale partial differential equations encountered in heat transfer, wave propagation, and coupled multi-physics problems.

Future work will extend the proposed adaptive framework to higher-dimensional problems, inverse parameter identification, and coupled thermo-mechanical systems, as well as explore integration with neural operator architectures for parametric and real-time prediction.

References

[1] A. Khosravirad, M. B. Ayani, Comparative analysis of thermal damage to laser-irradiated breast tumor based on Fourier conduction and non-Fourier heat conduction models: A numerical study, *International Communications in Heat and Mass Transfer,* Vol. 145, pp. 106837, 2023.

[2] D. Maillet, A review of the models using the Cattaneo and Vernotte hyperbolic heat equation and their experimental validation, *International Journal of Thermal Sciences,* Vol. 139, pp. 424-432, 2019.

[3] Y. Mao, Non-Fourier heat conduction of nano-films under ultra-fast laser, *Materials,* Vol. 16, No. 14, pp. 4988, 2023.

[4] M. M. Tung, Modeling the heating of biological tissue based on the hyperbolic heat transfer equation, *Mathematical and Computer Modelling,* Vol. 50, No. 5-6, pp. 665-672, 2009.

[5] C. Cattaneo, Sur une forme de l'equation de la chaleur eliminant la paradoxe d'une propagation instantantee, *Compt. Rendu,* Vol. 247, pp. 431-433, 1958.

[6] P. Vernotte, Les paradoxes de la theorie continue de l'equation de la chaleur, *Comptes rendus,* Vol. 246, pp. 3154, 1958.

[7] B. B. Xu, X. W. Gao, M. Cui, High precision simulation and analysis of non-Fourier heat transfer during laser processing, *International Journal of Heat and Mass Transfer,* Vol. 178, pp. 121574, 2021.

[8] S. Saedodin, M. J. Noroozi, D. D. Ganji, Nonlinear Analysis of a One-Dimensional Non-Fourier Heat Conduction Problem, *Proceedings of the National Academy of Sciences, India Section A: Physical Sciences,* Vol. 87, No. 3, pp. 447-454, 2017.

[9] R. Cai, C. Gou, H. Li, Algebraically explicit analytical solutions of unsteady 3-D nonlinear non-Fourier (hyperbolic) heat conduction, *International Journal of Thermal Sciences,* Vol. 45, No. 9, pp. 893-896, 2006.

[10] R. Shirmohammadi, A. Moosaie, Non-Fourier heat conduction in a hollow sphere with periodic surface heat flux, *International Communications in Heat and Mass Transfer,* Vol. 36, No. 8, pp. 827-833, 2009.

[11] S. C. Mishra, H. Sahai, Analyses of non-Fourier heat conduction in 1-D cylindrical and spherical geometry - An application of the lattice Boltzmann method, *International Journal of Heat and Mass Transfer,* Vol. 55, No. 23-24, pp. 7015-7023, 2012.

[12] H. Rahideh, P. Malekzadeh, M. R. Golbahar Haghighi, Non-Fourier Heat Conduction Analysis with Temperature-Dependent Thermal Conductivity, *International Scholarly Research Notices,* Vol. 2011, No. 1, pp. 321605, 2011.

[13] L. Wang, J. Xu, J. Wang, A peridynamic framework and simulation of non-Fourier and nonlocal heat conduction, *International Journal of Heat and Mass Transfer,* Vol. 118, pp. 1284-1292, 2018.

[14] W. Zhuoxin, Non-Fourier heat conduction analysis of a 2-D plate with inner cracks at arbitrary direction angles, *Chinese Journal of Aeronautics,* Vol. 35, No. 3, pp. 537-549, 2022.

[15] S. L. Brunton, J. N. Kutz, Methods for data-driven multiscale model discovery for materials, *Journal of Physics: Materials,* Vol. 2, No. 4, pp. 044002, 2019.

[16] S. L. Brunton, B. R. Noack, P. Koumoutsakos, Machine learning for fluid mechanics, *Annual Review of Fluid Mechanics,* Vol. 52, pp. 477-508, 2020.

[17] V. Yaghoubi, CNN-DST: ensemble deep learning based on Dempster-Shafer theory for vibration-based fault recognition, *arXiv preprint arXiv:2110.07191*, 2021.

[18] V. Yaghoubi, An ensemble classifier for vibration-based quality monitoring, *Mechanical Systems and Signal Processing,* Vol. 165, pp. 108341, 2022.

[19] H. Jin, E. Zhang, H. D. Espinosa, Recent advances and applications of machine learning in experimental solid mechanics: A review, *Applied Mechanics Reviews,* Vol. 75, No. 6, pp. 061001, 2023.

[20] J. Krzywanski, Heat and mass transfer prediction in fluidized beds of cooling and desalination systems by AI approach, *Applied Thermal Engineering,* Vol. 225, pp. 120200, 2023.

[21] A. Fallah, M. M. Aghdam, Physics-informed neural network for bending and free vibration analysis of three-dimensional functionally graded porous beam resting on elastic foundation, *Engineering with Computers,* Vol. 40, No. 1, pp. 437-454, 2024.

[22] M. Raissi, P. Perdikaris, G. E. Karniadakis, Physics-informed neural networks: A deep learning framework for solving forward and inverse problems involving nonlinear partial differential equations, *Journal of Computational Physics,* Vol. 378, pp. 686-707, 2019.

[23] A. Fallah, M. M. Aghdam, *Physics-Informed Neural Network for Solution of Nonlinear Differential Equations*, in: R. N. Jazar, L. Dai, *Nonlinear Approaches in Engineering Application: Automotive Engineering Problems*, Eds., pp. 163-178, Cham: Springer Nature Switzerland, 2024.

[24] E. Haghighat, A physics-informed deep learning framework for inversion and surrogate modeling in solid mechanics, *Computer Methods in Applied Mechanics and Engineering,* Vol. 379, pp. 113741, 2021.

[25] L. Wu, N. G. Kilingar, L. Noels, A recurrent neural network-accelerated multi-scale model for elasto-plastic heterogeneous materials subjected to random cyclic and non-proportional loading paths, *Computer Methods in Applied Mechanics and Engineering,* Vol. 369, pp. 113234, 2020.

[26] S. S. Mirsadeghi Esfahani, A. Fallah, M. Mohammadi Aghdam, Physics-Informed Neural Network for Nonlinear Bending Analysis of Nano-Beams: A Systematic Hyperparameter Optimization, *Mathematical and Computational Applications,* Vol. 30, pp. 72, 2025.

[27] S. S. Mirsadeghi Esfahani, A. Fallah, M. Mohammadi Aghdam, Physics-informed Neural Network for Bending Analysis of Two-Dimensional Functionally Graded Nano-Beams based on Nonlocal Strain Gradient Theory, *Journal of Computational Applied Mechanics,* Vol. 56, No. 1, pp. 222-248, 2025.

[28] R. Nopour, A. Fallah, M. M. Aghdam, Large deflection analysis of functionally graded reinforced sandwich beams with auxetic core using physics-informed neural network, *Mechanics Based Design of Structures and Machines,* Vol. 53, No. 7, pp. 5264-5288, 2025.

[29] X. Zhuang, Deep autoencoder based energy method for the bending, vibration, and buckling analysis of Kirchhoff plates with transfer learning, *European Journal of Mechanics - A/Solids,* Vol. 87, pp. 104225, 2021.

[30] S. Cai, Physics-informed neural networks for heat transfer problems, *Journal of Heat Transfer,* Vol. 143, No. 6, pp. 060801, 2021.

[31] A. Hazra, P. Sarkar, S. Sarkar, PINN-based estimation of convective heat transfer in jet impingement cooling, *Applied Thermal Engineering*, pp. 129088, 2025.

[32] T. Lu, Gradient-Driven Physics Informed Neural Networks for Conduction Heat Transfer and Incompressible Laminar Flow, *Journal of Computational and Nonlinear Dynamics,* Vol. 21, No. 4, 2025.

[33] O. Fuks, H. A. Tchelepi, Limitations of physics informed machine learning for nonlinear two-phase transport in porous media*,* Vol. 1, No. 1, pp. 19-37, 2020.

[34] T. Zhang, Application of Fourier feature physics-information neural network in model of pipeline conveying fluid, *Thin-Walled Structures,* Vol. 198, pp. 111693, 2024.

[35] M. Tancik, Fourier features let networks learn high frequency functions in low dimensional domains, *Advances in Neural Information Processing Systems,* Vol. 33, pp. 7537-7547, 2020.

[36] K. Chandan, Predicting the thermal distribution in a convective wavy fin using a novel training physics-informed neural network method, *Scientific Reports,* Vol. 14, No. 1, pp. 7045, 2024.

[37] P. Cui, Solution and applications of parameterized convective heat transfer equations using physics-informed neural networks, *International Journal of Heat and Mass Transfer,* Vol. 247, pp. 127040, 2025.

[38] J. Lee, Extended multiphysics-informed neural network for conjugate heat transfer problems, *International Journal of Heat and Mass Transfer,* Vol. 246, pp. 127098, 2025.

[39] J. Z. Peng, Physics-informed graph convolutional neural network for modeling fluid flow and heat convection, *Physics of Fluids,* Vol. 35, No. 8, 2023.

[40] J. Xu, H. Wei, H. Bao, Physics-informed neural networks for studying heat transfer in porous media, *International Journal of Heat and Mass Transfer,* Vol. 217, pp. 124671, 2023.

[41] S. Shi, D. Liu, Z. Zhao, Non-Fourier Heat Conduction based on Self-Adaptive Weight Physics-Informed Neural Networks, in *2021 40th Chinese Control Conference (CCC)*, 2021.

[42] J. Zheng, F. Li, H. Huang, T-phPINN: Physics-informed neural networks for solving 2D non-Fourier heat conduction equations, *International Journal of Heat and Mass Transfer,* Vol. 235, pp. 126216, 2024.

[43] Q. A. Huhn, M. E. Tano, J. C. Ragusa, Physics-Informed Neural Network with Fourier Features for Radiation Transport in Heterogeneous Media, *Nuclear Science and Engineering,* Vol. 197, No. 9, pp. 2484-2497, 2023.

[44] O. Sallam, M. Fürth, On the use of Fourier Features-Physics Informed Neural Networks (FF-PINN) for forward and inverse fluid mechanics problems, *Proceedings of the Institution of Mechanical Engineers, Part M: Journal of Engineering for the Maritime Environment,* Vol. 237, No. 4, pp. 846-866, 2023.